












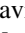


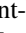



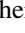









DESI Survey Validation Data in the COSMOS/Hyper Suprime-Cam Field: Cool Gas Trace Main-sequence Star-forming Galaxies at the Cosmic Noon

Siwei Zou^{1,2} , Linhua Jiang¹ , Zheng Cai² , John Moustakas³ , Zechang Sun² , Zhiwei Pan¹ , Jiani Ding^{4,5} , Jaime E. Forero-Romero⁶ , Hu Zou⁷ , Yuan-sen Ting^{8,9} , Matthew Pieri¹⁰ , Steven Ahlen¹¹ , David Alexander¹² , David Brooks¹³ , Arjun Dey¹⁴ , Andreu Font-Ribera¹⁵ , Satya Gontcho A. Gontcho¹⁶ , Klaus Honscheid^{17,18} , Martin Landriau¹⁶ , Axel de la Macorra¹⁹ , Mariana Vargas Magana¹⁹ , Aaron Meisner¹⁴ , Ramon Miquel^{15,20} , Michael Schubnell²¹ , Gregory Tarlé²² , and Zhimin Zhou⁷ 

¹ Kavli Institute for Astronomy and Astrophysics, Peking University, Beijing 100871, People's Republic of China; siwei1905@gmail.com

² Department of Astronomy, Tsinghua University, Beijing 100084, People's Republic of China

³ Department of Physics and Astronomy, Siena College, 515 Loudon Road, Loudonville, NY 12211, USA

⁴ Department of Astronomy and Astrophysics, University of California, Santa Cruz, 1156 High Street, Santa Cruz, CA 95065, USA

⁵ University of California Observatories, 1156 High Street, Santa Cruz, CA 95065, USA

⁶ Departamento de Física, Universidad de los Andes, Cra. 1 No. 18A-10, Edificio Ip, CP 111711, Bogotá, Colombia

⁷ National Astronomical Observatories, Chinese Academy of Sciences, A20 Datun Road, Chaoyang District, Beijing 100012, People's Republic of China

⁸ Research School of Astronomy & Astrophysics, Australian National University, Cotter Road, Weston, ACT 2611, Australia

⁹ School of Computing, Australian National University, Acton, ACT 2601, Australia

¹⁰ Aix Marseille Univ, CNRS, CNES, LAM, Marseille, France

¹¹ Physics Dept., Boston University, 590 Commonwealth Avenue, Boston, MA 02215, USA

¹² Centre for Extragalactic Astronomy, Department of Physics, Durham University, South Road, Durham, DH1 3LE, UK

¹³ Department of Physics & Astronomy, University College London, Gower Street, London, WC1E 6BT, UK

¹⁴ NSF's NOIRLab, 950 N. Cherry Avenue, Tucson, AZ 85719, USA

¹⁵ Institut de Física d'Altes Energies (IFAE), The Barcelona Institute of Science and Technology, Campus UAB, E-08193 Bellaterra, Barcelona, Spain

¹⁶ Lawrence Berkeley National Laboratory, 1 Cyclotron Road, Berkeley, CA 94720, USA

¹⁷ Department of Physics, The Ohio State University, 191 West Woodruff Avenue, Columbus, OH 43210, USA

¹⁸ Center for Cosmology and AstroParticle Physics, The Ohio State University, 191 West Woodruff Avenue, Columbus, OH 43210, USA

¹⁹ Instituto de Física, Universidad Nacional Autónoma de México, Cd. de México C.P. 04510, Mexico

²⁰ Institució Catalana de Recerca i Estudis Avançats, Passeig de Luíls Companys, 23, E-08010 Barcelona, Spain

²¹ Department of Physics, University of Michigan, Ann Arbor, MI 48109, USA

²² University of Michigan, Ann Arbor, MI 48109, USA

Received 2023 February 23; revised 2023 November 2; accepted 2023 November 3; published 2023 December 20

Abstract

We present the first result in exploring the gaseous halo and galaxy correlation using the Dark Energy Spectroscopic Instrument survey validation data in the Cosmic Evolution Survey (COSMOS) and Hyper Suprime-Cam field. We obtain multiphase gaseous halo properties in the circumgalactic medium by using 115 quasar spectra (signal-to-noise ratio > 3). We detect Mg II absorption at redshift $0.6 < z < 2.5$, C IV absorption at $1.6 < z < 3.6$, and H I absorption associated with the Mg II and C IV. By crossmatching the COSMOS2020 catalog, we identify the Mg II and C IV host galaxies in 10 quasar fields at $0.9 < z < 3.1$. We find that within the impact parameter of 250 kpc, a tight correlation is seen between the strong Mg II equivalent width and the host galaxy star formation rate. The covering fraction f_c of the strong Mg II selected galaxies, which is the ratio of the absorbing galaxy in a certain galaxy population, shows significant evolution in the main-sequence galaxies and marginal evolution in all the galaxy populations within 250 kpc at $0.9 < z < 2.2$. The f_c increase in the main-sequence galaxies likely suggests the coevolution of strong Mg II absorbing gas and the main-sequence galaxies at the cosmic noon. Furthermore, Mg II and C IV absorbing gas is detected out of the galaxy virial radius, tentatively indicating the feedback produced by the star formation and/or the environmental effects.

Unified Astronomy Thesaurus concepts: [Circumgalactic medium \(1879\)](#); [Galaxy environments \(2029\)](#); [Star formation \(1569\)](#); [Quasar absorption line spectroscopy \(1317\)](#)

1. Introduction

The baryon cycle in and around a galaxy is of critical importance in understanding the cosmic star formation history and galaxy evolution. The so-called interstellar medium (ISM) and circumgalactic medium (CGM) play a key role in regulating the baryon cycle and thus galaxy evolution (see the reviews of Tumlinson et al. 2017; Péroux & Howk 2020 and the references therein). The absorption lines produced by the intervening

medium toward bright background quasars provide a sensitive measurement of the multiphase gas properties in the transverse direction of the gaseous halos. Different phases (density, temperature, and ionization parameter) of the gas in the ISM and CGM can be characterized by different ions. For instance, neutral atomic carbon (C I) is used to trace cold, metal-enriched (Ledoux et al. 2015; Zou et al. 2018) and molecular gas (Noterdaeme et al. 2018). The Ly α absorption systems can probe optically thick neutral gas, known as damped Ly α (DLA) systems (neutral hydrogen column density $N(\text{H I}) > 10^{20.3} \text{ cm}^{-2}$; Petitjean et al. 2000; Wolfe et al. 2005; Prochter et al. 2006; Noterdaeme et al. 2011; Rafelski et al. 2012; Krogager et al. 2017; Neeleman et al. 2019; Lin et al. 2023). Mg II ($\lambda\lambda$ 2796, 2803) and

C IV doublets are found to reside in the cool ($T \sim 10^4$ K; Bergeron & Boissé 1991; Steidel et al. 2002) and warm-hot gas ($T \sim 10^{5.5-6}$ K) gas, respectively (Bordoloi et al. 2014a; Burchett et al. 2016). Additionally, the peculiar abundance patterns of DLA or Lyman-limit systems potentially exhibit the signatures of the old generation of stars (e.g., Zou et al. 2020; Welsh et al. 2022).

Extensive experiments have been designed to explore the CGM-galaxy correlation and its role in galaxy evolution at redshift $z < 1$. The CGM has been found to corotate with the host galaxy along the major and minor axis (Nielsen et al. 2013b). The strength (equivalent width or column density) of the cool gas tentatively correlates with the luminosity (L_B of the host galaxy; Chen et al. 2010a) and is anticorrelated with the impact parameter of the galaxy (Bouché et al. 2006; Nielsen et al. 2013a). Emission from the diffuse gas region has also been detected in recent work (e.g., Feltre et al. 2018; Leclercq et al. 2022).

Observations are still limited in exploring the CGM-galaxy correlation at $z > 1$ because direct galaxy observation is very challenging for ground-based telescopes. The stacking of a large quantity of Sloan Digital Sky Survey (SDSS) quasar spectra can be used to probe the weak galaxy emission at high redshift (Joshi et al. 2017) and CGM distribution at a large scale (Pieri et al. 2014). Recently, integral field spectroscopy, such as that involving the Keck Cosmic Web Imager and Very Large Telescope (VLT)/Multi Unit Spectroscopic Explorer (MUSE), has offered an efficient tool for providing a 3D view of both the large and small scale of the CGM at $z < 1.5$ and $z > 2$. Samples of Mg II-galaxy pairs at $z < 1.5$ are built using VLT/MUSE (Schroetter et al. 2019, 2021; Zabl et al. 2019; Dutta et al. 2020). A bimodality of the azimuthal angle-metallicity relation has been found in the MusE GAs FLOW and Wind (MEGAFLOW) survey and at $z \sim 1$ to trace either inflow (Zabl et al. 2019) or galactic outflow (Schroetter et al. 2019). The environmental effects of cool gas traced by Mg II have been reported in the MUSE Analysis of Gas around Galaxies (MAGG) survey (Dutta et al. 2020).

At $z = 2-4$, the CGM can be probed by the emission lines near bright quasars (e.g., Cantalupo et al. 2014; Martin et al. 2014; Cai et al. 2019; Fossati et al. 2021) and overdense regions (Cai et al. 2017a, 2017b). Surveys to study the small-scale CGM structure and its correlation with the host galaxy (ies) are somehow scarce (e.g., the Keck Baryonic Structure Survey; Rudie et al. 2012, 2019). The cosmic star formation rate (SFR) and baryon accretion peak around $z \sim 2$ (Madau & Dickinson 2014). In order to trace the multiphase gas-galaxy coevolution at $z = 1-3$, especially toward the cosmic noon ($z = 2-3$), we present a pilot study that takes advantage of the 30 multiband photometry in the Cosmological Evolution Survey (COSMOS) field to search for the CGM host galaxies. In Zou et al. (2021; hereafter Z21), the authors tentatively search for strong Mg II absorber ($2 < z < 6$) counterparts from Hubble Space Telescope/Canada-France-Hawaii Telescope/The Dark Energy Camera Legacy Survey deep images. The result indicates that the strong Mg II absorbing gas tends to have a smaller halo size, but a more disturbed environment than that at lower redshift.

In this paper, we will first present CGM gas properties by using the quasars observed in the Dark Energy Spectroscopic Instrument (DESI) survey validation (SV) in the COSMOS and Hyper Suprime-Cam (HSC) Subaru Strategic Program fields, then we will particularly study the CGM-galaxy correlation in

the COSMOS field. This paper is presented as follows: we introduce the observations and data analysis in Section 2. The multiphase gas properties are presented in Section 3, and the gas-galaxy correlation is presented in Section 4. We discuss and summarize the implications of this work in Sections 5 and 6.

2. Observations and Data Processing

DESI is a Stage IV ground-based dark energy experiment that studies baryon acoustic oscillations and the growth of structure through redshift-space distortions with a wide-area galaxy and quasar redshift survey (DESI Collaboration et al. 2016a, 2016b, 2022). Full details of the DESI early data release (EDR) and secondary projects are described in DESI Collaboration et al. (2023a, 2023b). Descriptions of the SV data and data reduction pipeline are presented in Myers et al. (2023) and Guy et al. (2023), respectively. Target selection and samples of quasars, bright galaxies, emission-line galaxies, and luminous red galaxies from the SV data can be found in Yèche et al. (2020), Chaussidon et al. (2023), Lan et al. (2023), Raichoor et al. (2023), Yang et al. (2023), and Zhou et al. (2023). The full Mg II absorber catalog of the DESI EDR data is presented in Napolitano et al. (2023).

This project is a DESI secondary program in the SV. The quasars are selected from the overlapping region of the COSMOS and HSC ultra-deep (Aihara et al. 2018) fields (2 deg^2 and having the tangent point R.A., decl. at 150.116, 2.210). The observations of quasars in this work were conducted at Kitt Peak by DESI between 2021 March and May. The average effective exposure time is around 5.5 hr. The DESI SV quasar catalog is created with three algorithms: the DESI pipeline classifier Redrock (RR; S. Bailey et al. 2023, in preparation), a broad Mg II line finder, and a machine-learning-based classifier QuasarNET (Busca & Balland 2018; Farr et al. 2020). The RR algorithm is a template-fitting classifier to classify the quasars using the templates of the different targets (stars, galaxies, and quasars) generated from SDSS spectra. The Mg II line finder is an afterburner algorithm using the inputs and outputs from RR. QuasarNET is a deep convolutional neural network classifier. Details of the quasar visual inspection results are presented in Alexander et al. (2023).

From all the observed quasars in the COSMOS/HSC field, we selected 115 quasars, each with a mean signal-to-noise ratio (S/N) greater than 3. We calculate the mean S/N of one spectrum as the mean S/N per pixel from three different intervals, where there are no significant emission and absorption lines (flux residuals smaller than 0.5). Details of all quasars used in this work are presented in the Appendix in Table A1. Among these 114 quasars, 30 quasars are included in the quasar catalog of SDSS DR 16 (Lyke et al. 2020) and the other 84 are new quasars. We show a spectra comparison for one quasar (J095749.98+013354.1), taken by DESI and SDSS, as presented in Figure 1. The DESI spectra resolution at 3600–9800 Å ranges from 2000 to 5000.

2.1. Normalization and Metal Lines Finder

To detect the intervening absorption systems, we first normalize the quasar spectrum by dividing the flux with the continuum. The continuum defined in this work is the spline line without a significant absorption feature (see the red curved line in Figure 1 for an example). We use two methods to

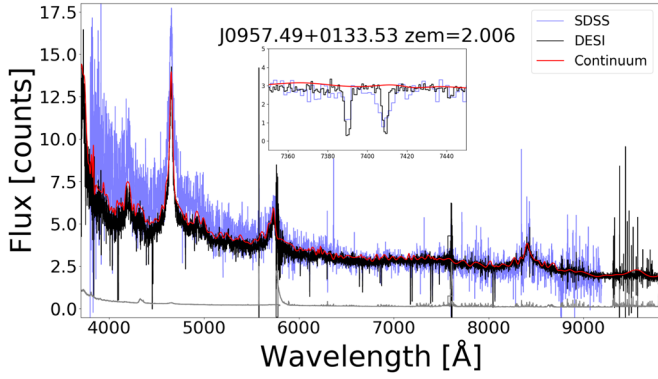


Figure 1. Spectra of J095749.98+013354.1 taken by DESI (black) and SDSS (blue), respectively. Zoom-in spectra are of one Mg II line detected at $z = 1.6428$. The exposure times of the DESI and SDSS observations are 7302 s and 4027 s, respectively. The red curve is the continuum fitting done by the method described in Section 2.1.

estimate the quasar continuum: the principal component analysis method (see, e.g., Pâris et al. 2011; Guo et al. 2018) and an unsupervised probabilistic continuum fitting method with uncertainty quantification (Sun et al. 2023).²³ The fitting spectra redward of the Ly α emission from these two methods are consistent. The fitting results are then visually checked to avoid any significant improper fitting.

After obtaining the normalized spectra, we use the algorithm described in Z21 to automatically search for metal lines redward of the Ly α emission, i.e., rest frame λ 1216–3000 Å. We briefly introduce the algorithm here. We identify the absorption feature from the normalized spectrum with a Gaussian kernel filter having a rest-frame velocity FWHM smaller than 600 km s⁻¹. When the rest-frame equivalent width W_r of this Gaussian kernel is greater than our detection limit (0.3 Å), this kernel is then identified as an absorption feature. We search for the Mg II (C IV) doublets with two Gaussian kernels that are separated around 770 km s⁻¹ (500 km s⁻¹). The self-blending of the Mg II and C IV systems can be mitigated by the two Gaussian kernels. We then visually inspect all the detected absorbers to ensure there is no significant blending from absorber systems at other redshifts. The error of the equivalent width is calculated by the flux variance summation over the search boxcar. We also add the S/N constraint in the nearby region of the absorption feature. The final absorber sample is visually checked. The criteria to select the Mg II (C IV) doublets are as follows.

(1) The local S/N > 3, where the local S/N is the mean S/N per pixel around ± 10 pixels adjacent to the search boxcar center; (2) $W_r(\lambda 2796) > 0.3$ Å and $W_r(\lambda 2803) > 0.15$ Å ($W_r(\lambda 1548) > 0.3$ Å and $W_r(\lambda 1550) > 0.15$ Å) for C IV; and (3) $W_r(\lambda 2796)/\sigma(W_r) > 3$ and $W_r(\lambda 2803)/\sigma(W_r) > 3$ ($W_r(\lambda 1548)/\sigma(W_r) > 3$ and $W_r(\lambda 1550)/\sigma(W_r) > 3$ for C IV), indicating a 3 σ detection.

3. Multiphase Gas

The multiplicity of the absorbers is detected (H I, Mg II, C IV, Al II, Al III, Si II, Si III, and Si IV) from the DESI SV quasar spectra. In this work, we focus on the discussion of H I, Mg II, and C IV. We detect Mg II and C IV independently using the algorithm described in Section 2.1; the H I systems are then

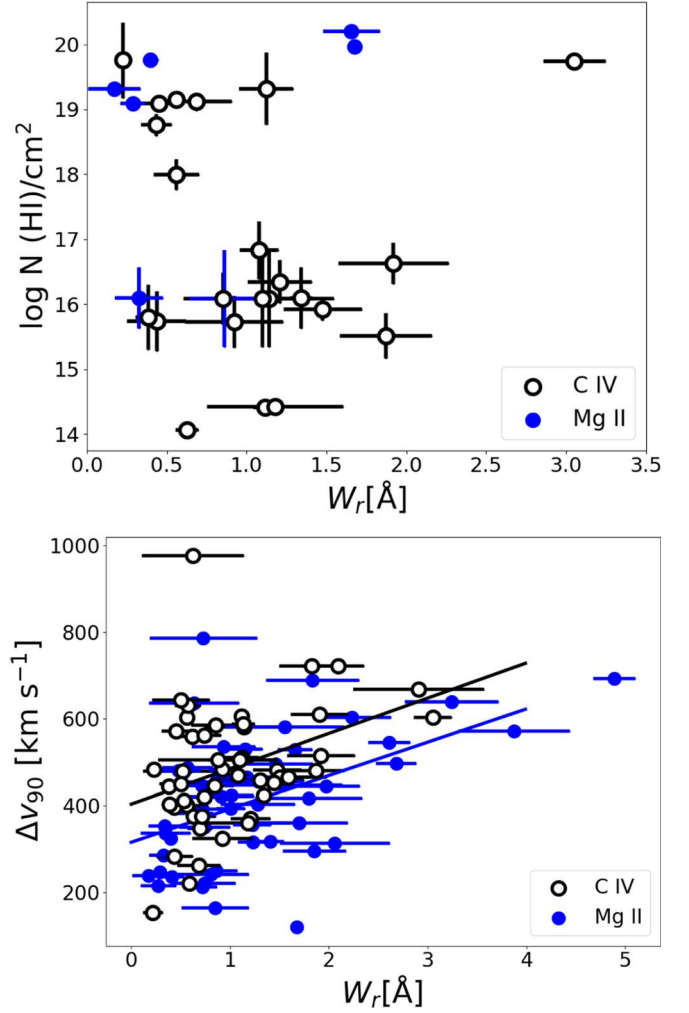


Figure 2. Upper: the column density of H I against the equivalent widths of Mg II (blue dots) and C IV (hollow black circles) where the three ions are detectable. All of the C IV and Mg II systems have $\log N(\text{H I})/\text{cm}^2 > 14.0$. The Mg II systems have relatively higher $N(\text{H I})$ than the C IV systems. Lower: the Δv_{90} - W_r relation of our detected Mg II and C IV absorbers. The Δv_{90} is the velocity spread encompassing 90% of the total optical depth of the absorption line. The Pearson coefficient p -value for the Δv of the Mg II and C IV absorbers is 0.024, indicating a similarity between these two variables.

searched in the same system once the Mg II or C IV have been detected.

Quantitatively, we detect 51 Mg II absorption ($0.66 < z < 2.49$, $0.27 < W_r < 4.89$ Å) and 50 C IV absorption ($1.35 < z < 3.18$, $0.22 < W_r < 3.05$ Å). In the overlapping redshift coverage between Mg II and H I ($z = 1.95$ –2.50); C IV and H I ($z = 1.95$ –3.20), 8 out of 10 (80%) Mg II systems have H I detection, and 24 out of 29 (82.75%) C IV systems have H I detection. In the redshift coverage of both Mg II and C IV ($z = 1.3$ –2.5), 20 out of 34 (58.82%) Mg II systems have C IV detection. We found a relatively larger median W_r of the C IV systems with Mg II absorption (0.859 Å) than the C IV systems without Mg II absorption (0.694 Å).

We plot all systems having H I detection in the upper panel of Figure 2. The figure indicates that all of the detected H I absorption associated with Mg II and C IV systems has $\log N(\text{H I})/\text{cm}^2 > 14.0$. The column density of H I is measured using the Voigt profile (the package Voigtfit; Krogager 2018) when there are strong Lyman series lines (e.g., $W_r(\lambda 1215) > 10$ Å) detected at the redshifts of the metal line

²³ <https://github.com/ZechangSun/QFA/>

absorber. The total column density of HI is derived from both the Ly α and Ly β lines (when detected). Both the Ly α and Ly β lines are fitted with the same Doppler parameter b , which is varied between 40 and 200 km s $^{-1}$. The final N value and its associated error are taken when the smallest χ^2 value is obtained. The complete fit results of the Mg II, C IV, and HI systems are presented in the Appendix in Table A2. This suggests that Mg II absorbers probe a relatively higher $N(\text{HI})$ gas than the C IV absorbers. All of the Mg II systems have $\log N(\text{HI})/\text{cm}^2 > 16.0$, which is consistent with what previous detections have claimed for Mg II absorption at $z < 1$ (e.g., Churchill et al. 2000; Nielsen et al. 2013b). In particular, five out of seven (71.43%) Mg II systems are associated with DLA and sub-DLA ($19.0 < \log N(\text{HI})/\text{cm}^2 < 20.3$) systems, indicating a significant correlation between Mg II systems and large $N(\text{HI})$ gas. The C IV systems are likely to probe a wider range of $N(\text{HI})$ gas than Mg II: one is associated with a more neutral phase having $18.5 < \log N(\text{HI})/\text{cm}^2 < 20$ and one is associated with a lower density phase ($14.0 < \log N(\text{HI})/\text{cm}^2 < 17.0$). Note that the system with the highest $N(\text{HI})$ has Mg II, but no 3σ C IV detection.

3.1. Line Density Evolution of Different Ions

In this paragraph, we present the statistical properties of the metal absorbers. First, we calculate the survey completeness by taking into account the contamination, such as the skylines and spikes in the spectra. To calculate the survey completeness, we follow and update the algorithm described in Z21. We briefly introduce the algorithm here. The method is to sample uniformly mock Mg II and C IV doublets in each spectrum using a Monte Carlo simulation. Then we use the detection algorithm in Section 2.1 to calculate the recovery rate. We generate 10,000 doublets with equivalent widths that vary and are uniformly distributed between 0.3 and 4.0 Å. We measure the real velocity spread of the absorption profile, Δv_{90} , defined as the velocity spread containing 90% of the total optical depth of the absorption line (e.g., Prochaska et al. 2008). We fit a relation between W_r and the velocity spread Δv_{90} with a polynomial curve fitting technique considering the errors from two variables of the Mg II and C IV absorbers: $\Delta v_{90} = 77 \times W_r(\lambda 2796) + 315 \text{ km s}^{-1}$ and $\Delta v_{90} = 81 \times W_r(\lambda 1548) + 403 \text{ km s}^{-1}$. The Δv_{90} - W_r relation of Mg II and C IV is plotted in the lower panel of Figure 2. The inserted observed velocity of the absorber is given by the Δv_{90} - W_r relation. We then insert the mock doublets in 10,000 uniformly distributed redshifts in our searching pathlength (0.5–2.6 for Mg II and 1.3–3.2 for C IV). The detection result of every inserted absorber is described as a Heaviside function $H(z, W_r)$. The path density $g(z, W_r)$ is the integral of $H(z, W_r)$ over the total sightline number N . The average completeness is then calculated by the average of path density $C = \int_{W_{\text{min}}}^{\infty} g(z, W_r)/N$ as a function of redshift and W_r limit. (see Figure 3).

After applying the survey completeness correction, we calculate the line density per redshift bin (dN/dz) of Mg II and C IV. The line density of Mg II and C IV follow the Poisson distribution (Zhu & Ménard 2013), thus the error of dN/dz is given by $1/\sqrt{N}$. The final line densities of Mg II are presented in Table 1 and Figure 4. We compare our calculated dN/dz of Mg II with other surveys at $z = 1$ –2 (Zhu & Ménard 2013) and $z > 2$ (Chen et al. 2017; Z21). Figure 4 clearly shows that the line density evolution of strong Mg II ($W_r > 1 \text{ Å}$) is consistent

with the cosmic star formation history from the local Universe to $z \sim 6$. In particular, the trend has a tentative turnover at $z \sim 2$. The line densities of weaker Mg II systems ($0.3 \text{ Å} < W_r < 0.6 \text{ Å}$, $0.6 \text{ Å} < W_r < 1.0 \text{ Å}$) increase with the increasing redshift from $z = 0.6$ to 2.5.

4. Absorbing Gas–Host Galaxy Correlation

In this section, we first discuss the method of identifying the absorbing gas host galaxy. We then discuss the correlation between the gas-phase properties (absorber strengths and ionization states) and the host galaxy properties (stellar mass, halo mass, virial radius, impact parameter, and SFR). 14 quasar fields among the whole sample (115 quasars) are covered by the COSMOS2020 catalog (Weaver et al. 2022). We focus on the gas–galaxy correlation in the following discussion of these 14 quasar fields. We compare our results with other surveys, such as the MAGIICAT (Churchill et al. 2013a, 2013b; Nielsen et al. 2013b) and the MEGAFLOW (Zabl et al. 2019; Schroetter et al. 2019, 2021) surveys (for Mg II) at $z < 1$ and $z = 1$ –1.5 and the Cosmic Origin Spectrograph (COS) survey (for C IV) at $z < 1$ for low-mass galaxies (Borthakur et al. 2013; Bordoloi et al. 2014a).

4.1. Galaxy Identification

The identification of the CGM gas host galaxies is one of the key processes in revealing the correlation between the multi-phase gas and the host galaxy(ies). To compare our result with the MUSE surveys, we search for galaxy candidates within a radius of $30''$ (257.51 kpc at $z = 2.0$) using the COSMOS2020 galaxy catalog (Weaver et al. 2022). COSMOS is a survey that contains half a million galaxies with a limiting magnitude of 27.2 AB in the F814W band. The radius of $30''$ is determined to match the MUSE field of view of $1'$. The sky coverage of our survey is 2 deg^2 . Galaxies are detected in the combined $zYJHK_s$ images from the Subaru and Visible Infrared Survey Telescope for Astronomy (VISTA) telescopes (Scoville et al. 2007; Laigle et al. 2016; Weaver et al. 2022). By adding in particular the ultra-VISTA DR4 data and HSC PDR2 (Aihara et al. 2018), the photometric redshift (z_{phot}) uncertainties in COSMOS2020 can match those of galaxies 0.7 mag brighter in COSMOS2015 (Laigle et al. 2016). The photometric redshift is measured by LePhare (Arnouts et al. 2002; Ilbert et al. 2006) and EAZY (Brammer et al. 2008). The likelihood distribution of the z_{phot} is given by the observed photometry and redshift $\mathcal{L}(\text{data} | z)$. The final z_{phot} is the median of the likelihood distribution (z_{pdf}) and the error bar is the 1σ interval. Details of the photo- z measurement are presented in Weaver et al. (2022). The galaxy stellar mass and SFR are computed using LePhare with the same configuration as COSMOS2015 (see Laigle et al. 2016). The template library generated from the stellar population synthesis models in Bruzual & Charlot (2003) is fitted to the observed photometry to obtain the galaxy properties. We adopt the “best” values in the catalog that are taken at the minimum χ^2 . The stellar mass and SFR uncertainties are within the 68% confidence level. In this work, we use THE FARMER v2.1 catalog.²⁴

The precision of z_{phot} is quantified with the difference between the spectroscopic redshift z_{spec} and photometric redshift: $\sigma = |z_{\text{phot}} - z_{\text{spec}}|/(1 + z_{\text{spec}})$. We measure the z_{phot}

²⁴ <http://cosmos2020.calet.org>

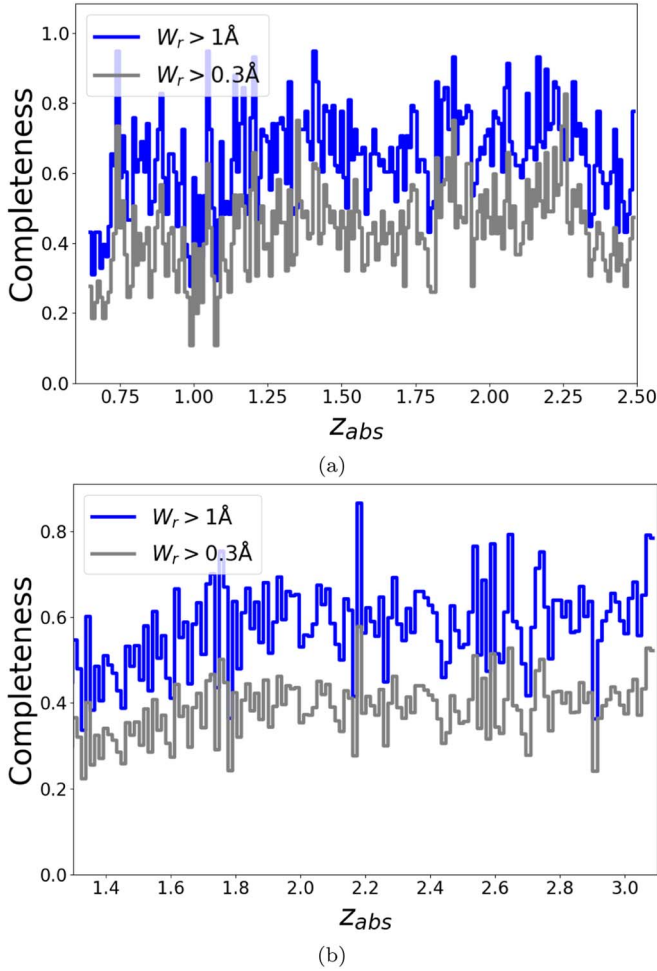


Figure 3. Average pathlength-weighted completeness as a function of the absorbing redshift (z_{abs}) of Mg II (upper) and C IV (lower) for 114 sightlines. The blue and gray curves are the completeness distribution with the equivalent width limits of $W_r \geq 1.0 \text{ \AA}$ and $W_r \geq 0.3 \text{ \AA}$, respectively.

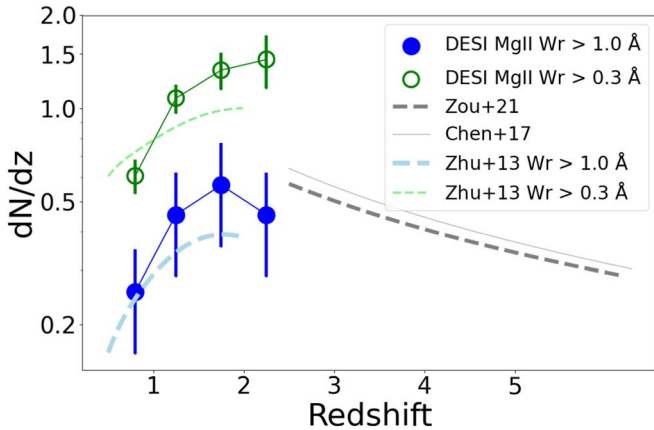


Figure 4. Line density dN/dz of the Mg II absorbers above 0.3 \AA (green circles) and 1.0 \AA (blue points) in this work. The gray dashed and solid lines are the fitting results of strong Mg II ($W_r > 1.0 \text{ \AA}$) at $2.2 < z < 6.0$ in Z21 and Chen et al. (2017), respectively. The strong Mg II line density evolution is consistent with the cosmic star formation evolution from $1.0 < z < 6.0$.

precision in the COSMOS field with the galaxy z_{spec} from DESI SV data. We find that the median σ is around 0.006. We select the absorbing gas host galaxies using criteria as follows: (a) $\sigma < 0.01$; and (b) we search the galaxy candidates within a

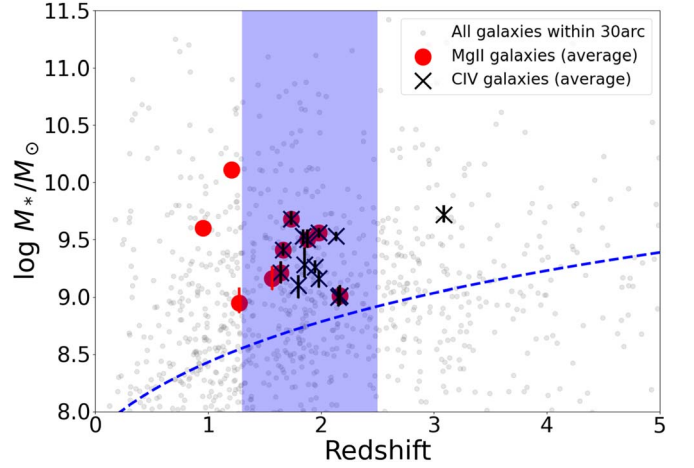


Figure 5. The stellar mass distribution of galaxies in the 14 sightlines covered by the COSMOS2020 catalog. The black curve is the stellar mass limit as a function of redshift from Weaver et al. (2022). The red dots are Mg II galaxy candidates, and the blue crosses are the C IV galaxy candidates. The gray dots are all galaxies within a $30'' \times 30''$ offset from the quasar. The blue rectangle is the detection redshift coverage of both Mg II and C IV.

$\pm 1000 \text{ km s}^{-1}$ velocity window with the absorber at z_{abs} in the center, i.e., $c \times |z_{\text{phot}} - z_{\text{abs}}| / (1 + z_{\text{abs}}) < 1000 \text{ km s}^{-1}$. Considering the photometric redshift uncertainty is still large for this velocity window ($\pm 1000 \text{ km s}^{-1}$), we include all the galaxies with a z_{pdf} distribution across this velocity window around the absorber's redshift, instead of finding the host galaxy. After applying these criteria, we preselected the Mg II and C IV host galaxy candidates. We plot all the preselected galaxy candidates in Figure 5. The blue dashed line in Figure 5 is the stellar mass completeness calculated in Weaver et al. (2022). We also test different galaxy selection criteria by cutting the stellar mass limit (the blue dashed line in Figure 5), SFR ($\log \text{SFR} > -1$), and L_v ($L_v/L_* > 0.01$, where L_v is the V-band luminosity and L_* is the characteristic galaxy luminosity at $z \sim 2$) limits, and find that the major result discussed in the following does not change.

4.2. Galaxy Counterpart Properties

We first present the Mg II and C IV host galaxies properties in this section. In Section 4.1, we select multiple galaxy candidates that are potentially associated with the absorbers. In order to minimize the uncertainty given by z_{phot} in finding the most likely absorber host galaxy, we measure a weighted average physical parameter (stellar mass, SFR, and impact parameter D) of all the galaxy candidates instead. The stellar mass, SFR, and luminosity contribution from a single galaxy candidate to the average parameter are weighted by their z_{phot} likelihood distribution area under the $\pm 1000 \text{ km s}^{-1}$ velocity window at the absorber redshift.

In Figure 6, we plot the M_* -SFR relation of Mg II and C IV absorbing galaxies. The blue hollow circles represent all the selected galaxy candidates colored by their z_{phot} distribution area probability within a velocity window of $\pm 1000 \text{ km s}^{-1}$ of the absorber. The filled blue circles are the weighted average parameters in each quasar field. The gray lines are the M_* -SFR relation of the main-sequence galaxies (MSGs) at $z = 1.6$ from Speagle et al. (2014) with 3 dexes of scatter. The preselected Mg II and C IV galaxies have stellar masses ranging from $10^{-8.5-11} M_\odot$. Most of the weighted stellar masses are in the $10^{9-10.5} M_\odot$ range.

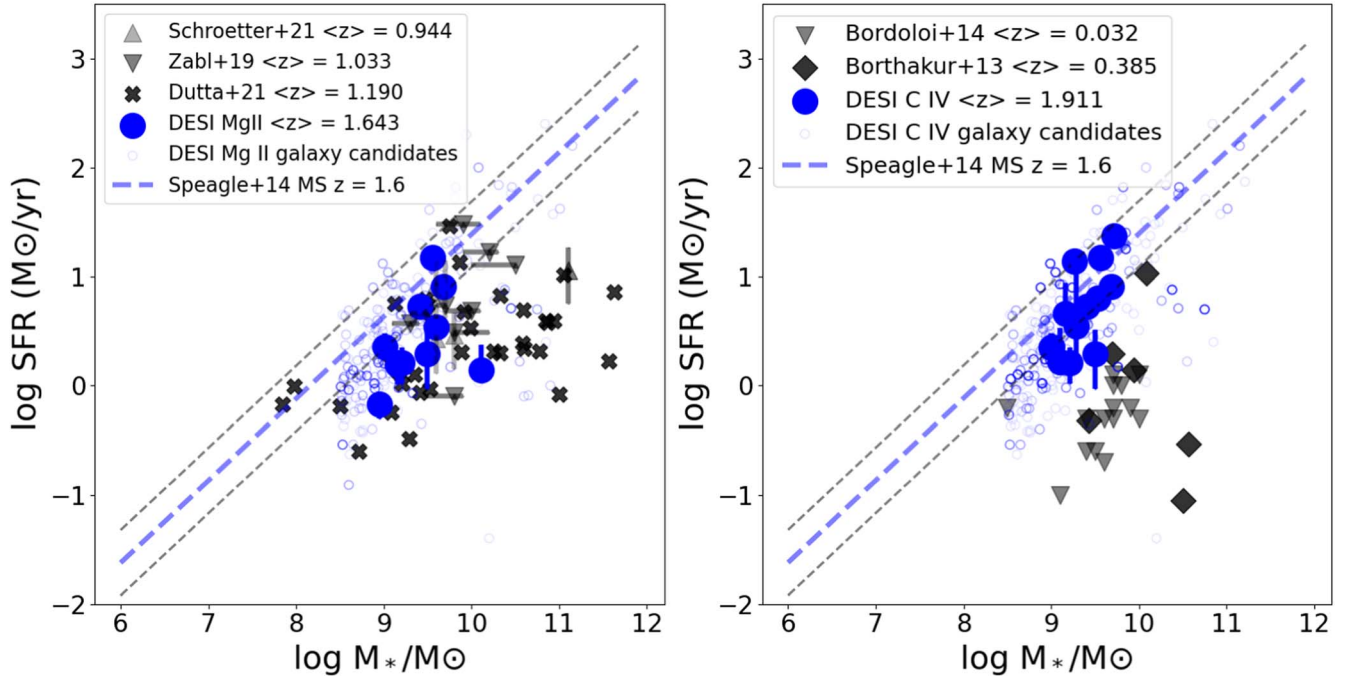


Figure 6. The SFR– M_* relation of Mg II (left) and C IV (right) host galaxies, respectively. The blue dashed line is the M_* –SFR relation of the MSGs at $z \sim 1.6$ with 0.3 dex scatter in Speagle et al. (2014). The blue dots are the average values of Mg II and C IV absorbing galaxies. Details of the method for obtaining the average values are described in Section 4.1. The hollow circles are the preselected galaxy candidates. Left: the black crosses are the Mg II galaxies from Dutta et al. (2020). The upward and downward triangles are the Mg II galaxies in Schroetter et al. (2021) and Zabl et al. (2019). Right: the black diamonds are the C IV galaxies in Borthakur et al. (2013) and the gray triangles are the C IV galaxies in Bordoloi et al. (2014a).

Table 1
Incidence Rate dN/dz and Comoving Density of Mg II and C IV Absorbers in This Work

Δz	Mg II dN/dz ($W_r > 0.3 \text{ \AA}$)	Mg II dN/dz ($W_r > 1.0 \text{ \AA}$)	Δz	C IV dN/dz ($W_r > 0.2 \text{ \AA}$)	C IV dN/dz ($W_r > 1.0 \text{ \AA}$)
0.60–1.00	0.606 ± 0.076	0.275 ± 0.127	1.30–1.50	1.675 ± 0.149	0.494 ± 0.094
1.00–1.50	1.079 ± 0.119	0.484 ± 0.293	1.50–2.00	1.549 ± 0.206	0.420 ± 0.122
1.50–2.00	1.330 ± 0.187	0.602 ± 0.141	2.00–2.50	2.311 ± 0.447	0.800 ± 0.298
2.00–2.50	1.440 ± 0.298	0.403 ± 0.149	2.50–3.20	3.689 ± 0.107	1.618 ± 0.799

4.3. Correlation between Gas and Galaxy Properties

We then explore the dependence of the absorbing gas strengths and ionization state on the host galaxy properties, such as SFR, M_* , V-band luminosity L_v , and the impact parameter D . Empirical correlations between the Mg II absorbing gas and host galaxy properties at $z < 1$ have been reported in the literature, such as the extent of the Mg II absorbing gas R_{gas} with the stellar mass relation (Chen et al. 2010b), the R_{gas} with the galaxy luminosity L_B relation (Chen et al. 2010a), and the W_r of Mg II and the luminosity of [O II] emission in the host galaxy relation, by stacking the SDSS spectra (Ménard et al. 2011) and the Mg II W_r – M_* relation (Bordoloi et al. 2011). The W_r – D anticorrelation is reported in extensive work (e.g., Nielsen et al. 2013a; Rubin et al. 2018), and the scatter in this relation is then explained by the segregation in the gas halo mass difference (Churchill et al. 2013a).

In Figures 7 and 8, we plot the weighted average W_r – M_* , W_r –SFR, W_r – L_v/L_\odot , and W_r – D/R_{vir} relations of the Mg II and C IV absorber and its host galaxies. The R_{vir} is the virial radius, defined by 200 times the overdensity of the critical cosmic density ρ_{crit} : $R_{\text{vir}} = (M_h/(3/4\pi)200 \rho_{\text{crit}})^{1/3}$. We calculate the

virial radius by converting the stellar mass into the halo mass using the stellar–halo mass relation in Girelli et al. (2020). We present the values of the weighted average galaxy parameters in Tables 2 and 3 as well.

We note that for Mg II, a tighter correlation is seen between the absorber strength with the average galaxy SFR than its luminosity and stellar mass. We assume a power-law correlation between W_r and SFR and L/L_* : $\log W_r(\text{Mg II}) = a \times \log(\text{SFR}) + b1$ and $\log W_r(\text{Mg II}) = a \times \log(L/L_*) + b2$. The maximum likelihood estimation result is $\log W_r(\text{Mg II}) = 0.14 \times \log(\text{SFR}) + 0.038$ (1σ). Different than the works in the local Universe, we do not see a significant correlation between the Mg II W_r against the stellar mass, D/R_{vir} , or luminosity within $D = 250$ kpc. Furthermore, we detect several Mg II systems at $D/R_{\text{vir}} > 1$.

For C IV, no significant correlations are seen between the overall C IV equivalent width and the galaxy candidates’ physical parameters. Additionally, we note that the C IV (with Mg II) systems’ and C IV-only systems’ host galaxies do not exhibit significant differences in M_* , SFR, or L_v . A marginal trend is seen where the C IV (no Mg II) systems tentatively reside in a larger impact parameter than the C IV (with Mg II) systems.

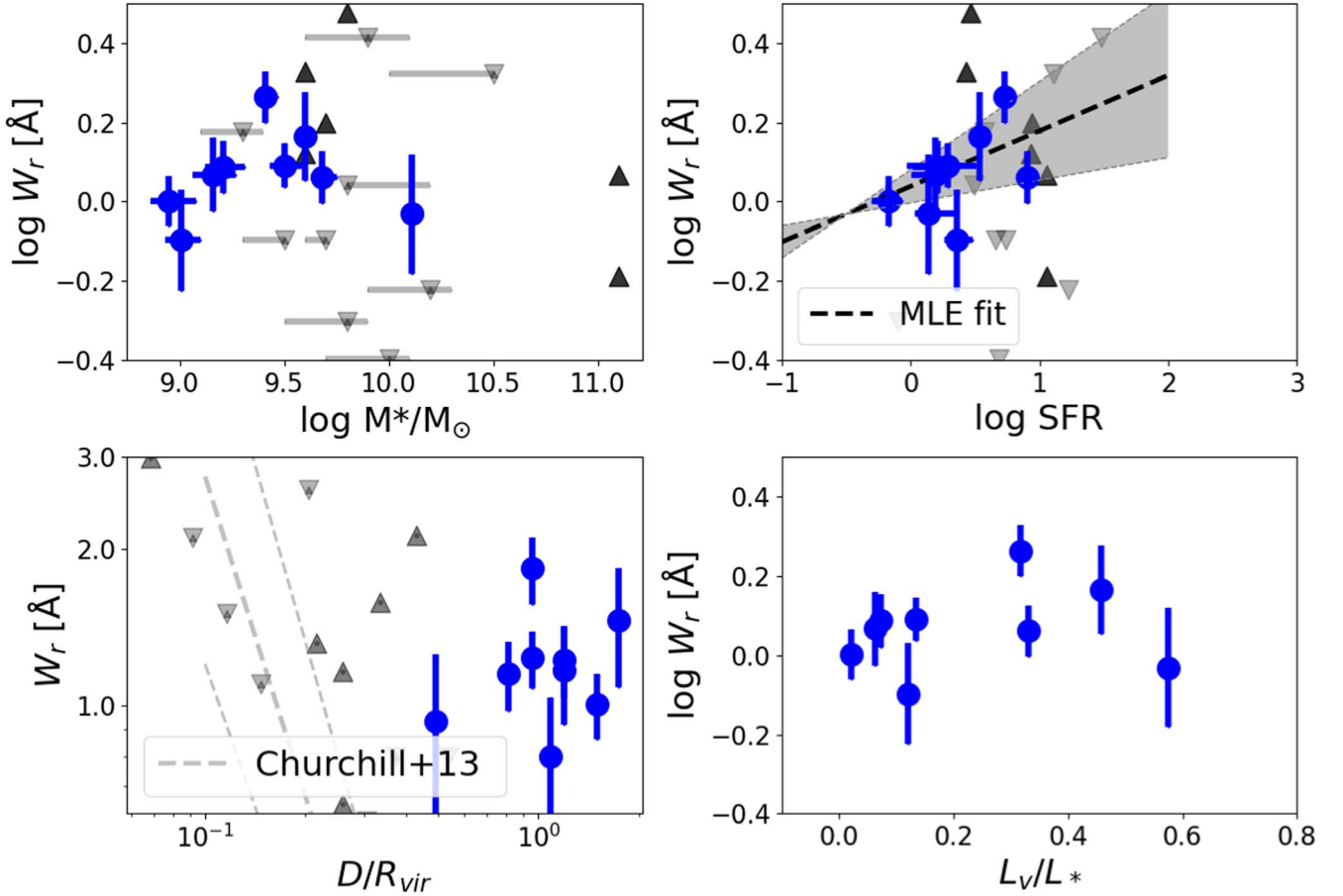


Figure 7. The Mg II absorbers' equivalent width dependence on the host galaxy properties. The labels for the data in each survey are consistent with the labels in the left panel of Figure 6. The upper panels show the W_r - M_* and W_r -SFR relations and the lower panels show the W_r - D/R_{vir} and W_r - L_v/L_* relations, respectively, indicative of a significant dependence of $W-r$ on the galaxy SFR. Different than what is found in Churchill et al. (2013a), the $W-r$ of strong Mg II at $z=1-2$ have a relatively constant dependence on the impact parameter D normalized by the virial radius R_{vir} . Note that we do not include the system having $W-r=0.28$ Å in this plot.

To further strengthen our results about the correlation between the absorber and its environment, we generate the posterior distribution $P(r|X)$ of the Pearson correlation coefficient r between $\log W_r$ - M_* , $\log W_r$ - \log SFR, and $\log W_r$ - L_v , where X is the galaxy data set. We assume there are n galaxies in one quasar field that are associated with the absorber. The $P(r|X) = \sum_{X_n} P(r|X_n)P(X_n|X)$. For one quasar field, we have n galaxies. We perform a Markov Chain Monte Carlo to sample the data set. We present the result in the Appendix in Figure A1. From the figure, we can tell that for Mg II, the W_r has a more significant correlation with SFR than stellar mass. For the C IV, no significant difference is seen between the W_r -SFR, W_r - M_* , and W_r - L_v/L_\odot relations. This is consistent with the results when including the major galaxy candidates. This method is unbiased in selecting the absorbing host galaxies with a velocity window and considering the z_{phot} uncertainties in a statistical way.

4.4. Covering Fraction of Mg II and C IV Absorbing Gas

Here we discuss the absorbing galaxy fraction among different galaxy populations above a certain detection limit. The covering fraction f_c within an impact parameter D is defined as the probability of a galaxy having a metal absorption line ($W_r > W_{lim}$) that can be detected. The probability can be calculated by the ratio of the absorbing galaxy number versus

the total galaxy number within a certain D (Bordoloi et al. 2014a):

$$f_c(W_r > W_{lim}) = \frac{N_{abs}}{N_{tot}},$$

for which N_{abs} is the number of galaxies having $W_r > W_{lim}$ galaxy number and N_{tot} is the total galaxy number in the same field. We use the same method to select the potential absorbing galaxies that are discussed in Section 4.1.

In our case, we count the number of absorbing galaxies weighted by the z_{pdf} distribution within the velocity window p_z of each galaxy. The median p_z in each quasar field is dominated by the galaxies that are most correlated with the absorber. We neglect the galaxies whose p_z is 1 dex smaller than the major galaxy(ies). We divide the differential Mg II and C IV absorbing galaxies' covering fraction at $0.9 < z < 2.2$ into three impact parameter bins (50–100, 100–200, and 200–250 kpc). The covering fraction is plotted in Figure 9. We find that within 250 kpc, an anticorrelation between the f_c and the D is seen for both Mg II and C IV. In Section 4, we show that the strength of our Mg II absorption has the most significant dependence on the SFR of the host galaxies, therefore we check the f_c of strong Mg II in the MSGs, $f_c(MSG) = N_{MgII}/N_{MSG}$. We select the MSGs based on the relation in Speagle et al. (2014) within 0.3 dex. The z_{pdf} of each galaxy is used for the target selection.

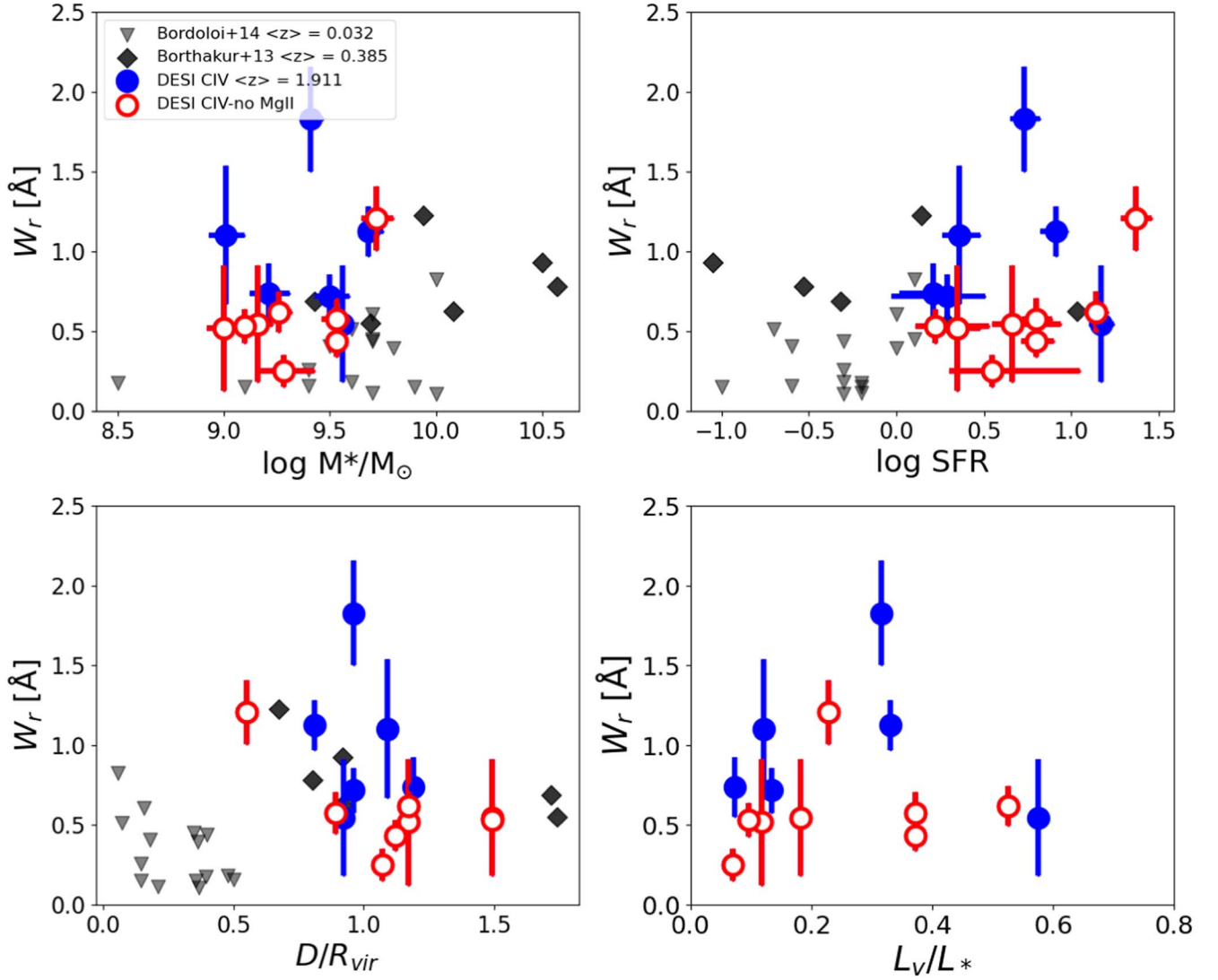


Figure 8. The C IV absorbers' equivalent width dependence on the host galaxy properties. The labels for the data in each survey are consistent with the labels in the right panel of Figure 6. The red circles are the C IV systems without Mg II absorption. The upper panels show the W_r - M_* and W_r -SFR relations and the lower panels show the W_r - D/R_{vir} and W_r - L_v/L_* relations, respectively. No significant correlation is found between the C IV strength and M_* , SFR, and D/R_{vir} . In particular, nearly half of our C IV galaxy D is beyond the virial radius.

Table 2
Mg II-absorbing Galaxy Candidates Information

QSO	R.A.	Decl.	D (kpc)	D/R_{vir}	z_{abs}	W_r (Å)	$\log(\text{SFR})$ ($M_\odot \text{ yr}^{-1}$)	$\log M^*/M_\odot$	L_v/L_*
J100219.49+015536.84	150.5812	1.9269	218.53	1.79	0.9520	1.462 ± 0.316	$0.54^{+0.07}_{-0.07}$	$9.6^{+0.04}_{-0.03}$	10.04
J100219.49+015536.84	150.5812	1.9269	102.62	0.31	1.2090	0.932 ± 0.260	$0.0^{+0.068}_{-0.068}$	$10.11^{+0.04}_{-0.03}$	10.14
J095834.03+024426.88	149.6418	2.7408	181.26	2.21	1.2756	1.005 ± 0.126	$-0.17^{+0.072}_{-0.297}$	$8.95^{+0.09}_{-0.13}$	8.7
J095749.98+013354.10	149.4582	1.5650	144.51	0.73	1.5660	1.169 ± 0.202	$0.19^{+0.18}_{-0.13}$	$9.16^{+0.10}_{-0.11}$	9.18
J095749.98+013354.10	149.4582	1.5650	153.39	0.73	1.6428	1.223 ± 0.162	$0.21^{+0.19}_{-0.14}$	$9.21^{+0.09}_{-0.10}$	9.24
J100031.61+014757.48	150.1317	1.7993	150.82	1.89	1.6625	1.836 ± 0.257	$0.73^{+0.08}_{-0.09}$	$9.41^{+0.05}_{-0.06}$	9.88
J095949.39+020140.80	149.9558	2.0280	137.37	0.74	1.7372	1.152 ± 0.175	$0.91^{+0.09}_{-0.07}$	$9.68^{+0.05}_{-0.07}$	9.9
J095749.98+013354.10	149.4582	1.5650	146.41	0.43	1.8770	1.234 ± 0.114	$0.29^{+1.262}_{-0.829}$	$9.50^{+0.07}_{-0.09}$	9.51
J100014.14+020054.36	150.0589	2.0151	149.83	1.85	1.9813	0.300 ± 0.117	$1.17^{+0.32}_{-0.22}$	$9.56^{+0.04}_{-0.04}$	10.14
J100105.30+021348.00	150.2703	2.2312	66.70	0.48	2.1680	0.800 ± 0.235	$0.36^{+0.1}_{-0.12}$	$9.01^{+0.08}_{-0.09}$	9.46

We present the fc results in Table 4. We find that the strong Mg II covering fraction in MSGs (the dark green circles) is 2 times higher (0.30 within 100 kpc) than that in the whole galaxy population (blue circles) in Figure 9. Given the

arbitrariness of the definition of MSGs within a 0.3 dex scatter and the uncertainties associated with estimating the main sequence, we further include two subsamples of galaxies with SFRs greater and smaller than the median SFR (the green and

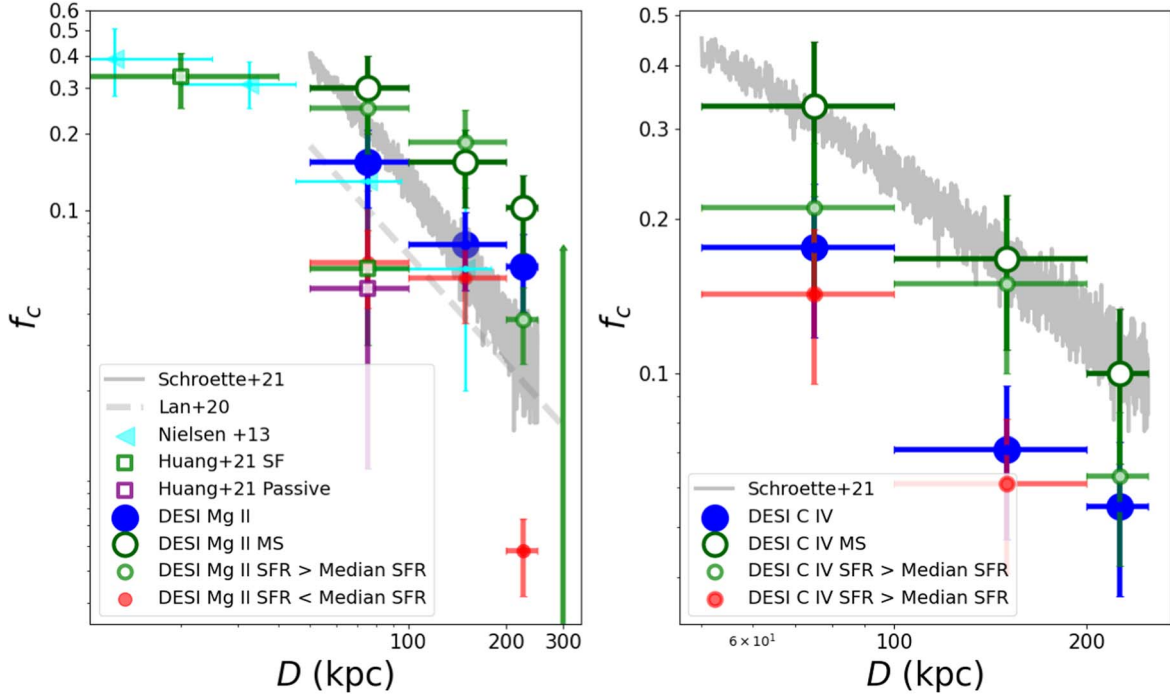


Figure 9. The covering fraction of Mg II ($z = 0.9\text{--}2.1$, $W_r \geq 1.0 \text{ \AA}$) and C IV absorbing gas ($z = 1.5\text{--}2.1$, $W_r \geq 0.5 \text{ \AA}$) in all galaxies (blue) and MSGs (dark green) as a function of the impact parameter D within 300 kpc. We also plot the covering fraction of absorbing galaxies in the subsamples with SFRs greater than the median SFR (smaller green circles) and those with SFRs less than the median SFR (red circles). The results of this work are calculated in three bins of D : 50–100 kpc, 100–200 kpc, and 200–250 kpc. The green and purple squares in the left panel are the f_c of Mg II ($W_r > 1.0 \text{ \AA}$) in star-forming and passive galaxies in Huang et al. (2021) and Chen et al. (2010a). The gray curves are the f_c distribution as a function (95% confidence region) of D in Schroetter et al. (2021) with a mean Mg II and C IV equivalent width of 0.99 and 0.70 \AA , respectively. The cyan triangles are the f_c of the strong Mg II ($> 1 \text{ \AA}$) absorbing gas in the MAGIICAT survey at $z < 1$ (Nielsen et al. 2013b). The gray dashed line is the f_c – D relation of the strong Mg II ($> 1 \text{ \AA}$) absorbing gas in Lan (2020).

Table 3
C IV–absorbing Galaxy Candidates Information

QSO	R.A.	Decl.	D (kpc)	D/R_{vir}	z_{abs}	W_r (\AA)	$\log(\text{SFR})$ ($M_{\odot} \text{ yr}^{-1}$)	$\log M^*/M_{\odot}$	Lv/L_{\odot}
J095749.98+013354.1	149.4582	1.5650	150.82	0.73	1.6428	0.738 ± 0.200	$0.21^{0.19}_{-0.14}$	$9.24^{9.37}_{9.15}$	9.24
J100031.61+014757.48	150.1317	1.7993	129.28	1.97	1.6625	1.828 ± 0.270	$0.73^{0.08}_{-0.09}$	$9.88^{9.66}_{9.55}$	9.88
J095949.39+020140.80	149.9558	2.0280	137.37	1.87	1.7372	1.126 ± 0.080	$0.91^{0.09}_{-0.07}$	$9.9^{10.16}_{10.03}$	9.9
J100302.90+015208.40	150.7621	1.8690	178.71	0.75	1.7970	0.531 ± 0.104	$0.22^{0.11}_{-0.31}$	$9.36^{8.83}_{8.6}$	9.36
J100014.14+020054.36	150.0589	2.0151	137.45	1.83	1.8400	0.574 ± 0.147	$0.8^{0.25}_{-0.5}$	$9.95^{8.23}_{7.94}$	9.95
J095834.03+024426.88	149.6418	2.7408	142.13	1.30	1.8555	0.252 ± 0.100	$0.55^{0.25}_{-0.5}$	$9.22^{9.12}_{8.81}$	9.22
J095749.98+013354.10	149.4582	1.5650	146.41	2.33	1.8770	0.716 ± 0.142	$0.29^{0.32}_{-0.22}$	$9.51^{10.54}_{10.38}$	9.51
J100014.14+020054.36	150.0589	2.0151	152.60	0.46	1.9450	0.620 ± 0.099	$1.14^{0.07}_{-0.07}$	$10.1^{9.12}_{8.97}$	10.1
J095752.30+022021.12	149.4679	2.3392	177.02	0.46	1.9810	0.546 ± 0.200	$0.66^{0.11}_{-0.28}$	$9.64^{8.87}_{8.62}$	9.64
J100014.14+020054.36	150.0589	2.0151	149.84	1.83	1.9813	0.453 ± 0.114	$1.17^{0.07}_{-0.07}$	$10.14^{9.12}_{8.97}$	10.14
J100014.14+020054.36	150.0589	2.0151	135.46	2.19	2.1305	0.434 ± 0.071	$0.80^{0.09}_{-0.1}$	$9.95^{11.08}_{10.98}$	9.95
J100105.30+021348.00	150.2721	2.2300	133.99	0.49	2.1530	0.518 ± 0.341	$0.35^{0.1}_{-0.13}$	$9.45^{9.432}_{9.314}$	9.45
J100105.30+021348.00	150.2721	2.2300	137.10	0.71	2.1680	1.102 ± 0.221	$0.36^{0.1}_{-0.12}$	$9.46^{9.432}_{9.314}$	9.46
J095806.96+022248.36	149.5209	2.3814	117.77	0.42	3.0880	1.207 ± 0.211	$1.37^{0.09}_{-0.09}$	$9.74^{8.74}_{8.67}$	9.74

Table 4
Covering Fraction of Mg II and C IV in All the Galaxies and MSGs at Different Impact Parameter Bins (50–100, 100–200, and 200–250 kpc), Respectively

D	f_c Mg II	f_c Mg II (MSG)	f_c C IV	f_c C IV (MSG)
50–100 kpc	0.152 ± 0.076	0.290 ± 0.127	0.176 ± 0.024	0.333 ± 0.083
100–200 kpc	0.074 ± 0.119	0.154 ± 0.293	0.071 ± 0.022	0.167 ± 0.051
200–250 kpc	0.061 ± 0.187	0.103 ± 0.141	0.055 ± 0.017	0.100 ± 0.038

Note. The galaxies are searched within a $30''$ offset from the quasar (absorbing system) using the COSMOS2020 catalog.

red circles in Figure 9). The f_c value of the Mg II galaxies in the subsample with $\text{SFR} > \text{median SFR}$ is similar to $f_c(\text{MSG})$ and exhibits a significant evolution compared to those in the local star-forming galaxies in Huang et al. (2021).

4.5. Comparison with Other Surveys

We compare our CGM–galaxy correlation results with other surveys in this section. We are cautious about comparing surveys having different depths and sample selection methods. Therefore we only discuss the trends here, rather than the quantitative differences.

For Mg II, we compare our results with the strong Mg II–galaxy correlation in MAGIICAT (Nielsen et al. 2013b), the MAGAFLOW survey (Schroetter et al. 2019; Zabl et al. 2019), and the DECaLS imaging survey (Lan 2020). The galaxies selected in MAGIICAT have a similar depth as ours (a B -band magnitude limit of -16.1 ; i.e., around 24.5 mag at $z = 0.34$). The DECaLS imagings used in Lan (2020) have g - and z -band limits of 24.2 and 23 mag, respectively. We perform a Kolmogorov–Smirnov test between the M_* –SFR relation of the sample and the M_* –SFR of galaxies in the MAGAFLOW inflowing mode (upward triangles) and outflowing mode (downward triangles). The p -values are 0.014 and 0.0153 , respectively, suggesting that our Mg II gas does not exhibit obvious inflowing or outflowing features. In other words, the strong Mg II gas at $z = 1–2$ tentatively exhibits complex kinematics, which may be a combination of effects of gas accretion, galactic outflows, and gas recycling, etc.

We compare the Mg II having $W_r > 1 \text{ \AA}$ gas f_c with that at $z = 1–1.5$ (Lan 2020; the gray dashed line and gray line, respectively) and $z < 1$ (Nielsen et al. 2013a; gray triangles). We note that the f_c of our strong Mg II absorbing gas shows a more marginal evolution than that at $z < 1$ (Nielsen et al. 2013a). The Mg II absorbing gas covering fraction in either MSGs or star-forming galaxies has a significant evolution from $z = 0$ to $z = 1–2.5$. Lan (2020) also finds that the covering fraction of strong Mg II systems in star-forming galaxies is higher than that in passive galaxies, exhibiting a significant evolution from $z = 0.4$ to $z = 1.3$. Schroetter et al. (2021) provide a novel Hamiltonian Monte Carlo model optimizing for estimating the f_c with limited samples. Their f_c is for Mg II systems having $W_r > 0.6 \text{ \AA}$; it is clear that our strong Mg II gas f_c is higher than their f_c beyond 100 kpc.

We compare our C IV M_* –SFR relation with C IV host galaxies from the COS-Dwarfs (Bordoloi et al. 2014b) and COS-Halo surveys (Borthakur et al. 2013) at $z < 1$. Bordoloi et al. (2014b) study a sample of 43 sub- L_* /dwarf galaxies at $z < 0.1$. A tentative correlation between the C IV W_r and host galaxy SFR has been reported in Bordoloi et al. (2014b) at $z < 1$. Borthakur et al. (2013) study 20 galaxies at $z < 0.2$ and find a high detection rate of C IV systems in starburst galaxies. The detection rate of C IV is four of five in starburst galaxies (the blue triangles in Figure 8) and 2 of 12 in the control sample comprising of normal/passive galaxies (gray triangles).

We note that our C IV f_c , unlike the strong Mg II gas, is lower than that in the MAGAFLOW survey (Schroetter et al. 2021) at $z = 1–1.5$ within 250 kpc. This may be because half of our C IV systems are Mg II-bearing halos, and the galaxies associated with weaker C IV-only halos are underestimated. In Schroetter et al. (2021), the authors suggest that at $z = 1–1.5$, the covering fraction of C IV-only gas is larger than that of

Mg II and C IV gas within 250 kpc and it likely resides a broader radius in the IGM (out to 250 kpc).

5. Discussion

5.1. Strong Mg II Absorbing Gas Contribution to Global SFR at $z = 1–2$

We follow the method described in Nestor et al. (2011) to estimate the strong Mg II gas contribution to the global SFR density:

$$F = \rho_{\text{SFR}}^{\text{MgII}} / \rho_{\text{SFR}} = \langle \text{SFR} \rangle \times \frac{dN}{dz} \frac{dl}{dz} \sigma^{-1} / \rho_{\text{SFR}},$$

where $\langle \text{SFR} \rangle$ is the mean SFR of Mg II host galaxies, the dN/dz is the line density of the Mg II absorbers, the dl/dz is the differential proper distance, σ is the Mg II gas cross section, and the ρ_{SFR} is the global star formation density. We take our detected strong Mg II galaxy $\langle \text{SFR} \rangle$ of $7.44 M_{\odot} \text{ yr}^{-1}$, the dN/dz at $1.5–2.0 = 0.753 \pm 0.141$, and the cross section of Mg II gas as $(250 \text{ kpc})^2$. The ρ_{SFR} at $z = 2.0$ calculated from Equation (15) in Madau & Dickinson (2014) is $0.132 M_{\odot} \text{ yr}^{-1} \text{ Mpc}^{-3}$. We then estimate the contribution of strong Mg II absorbing gas to the global SFR density at $z \sim 2.0$ is 0.068 by assuming a gas cross section of $(250 \text{ kpc})^2$. This fraction is consistent with our measured covering fraction of strong Mg II in the star-forming galaxy subsample within 250 kpc, further suggesting the coevolution of cool gas probed by the strong Mg II systems and the cosmic star formation activity.

5.2. Mg II and C IV Gas Origins

Here we discuss how the Mg II and C IV absorbing gas fuel the galaxy star formation and are affected by the galactic feedback toward the cosmic noon. According to the results above, we find that two gas phases coexist in the CGM in this work: one is with detectable Mg II and C IV absorption in the same system, i.e., the same physical position and sharing similar kinematics profiles, probing a relatively higher $N(\text{H I})$; and one is with the C IV-only systems, probing a lower $N(\text{H I})$ gas and a tentative larger impact parameter. Such a multiphase structure of the CGM is clearly seen in the hydrodynamic simulations (Ford et al. 2013; Suresh et al. 2017). In Ford et al. (2013), the simulation reveals that within the 300 kpc of galaxies at $z = 0.25$, the multiphase CGM generally probes a $10^{4–4.5} \text{ K}$ photoionized gas. Low ions, such as Mg II and Si IV, probe a denser gas and are closer to galaxies, while C IV can be associated with the cool gas in the inner region or the collisionally dominated highly ionized gas in a broader region. In this work, we mainly consider the CGM within 250 kpc of the galaxy; the gas mainly exhibits the “halo fountains” region properties suggested by the simulation of Oppenheimer & Davé (2008). This region is first fueled by the metal-poor inflowing gas, but later enriched by the metal-rich and momentum-driven outflows, where the gas has complex kinematics. Recent TNG simulations have the resolution to resolve small-scale structures. The Mg II halos are found to be highly structured, clumpy, asymmetric (Nelson et al. 2020), and with a variety of kinematics (DeFelippis et al. 2020). This likely explains why our Mg II absorbing gas does not exhibit obvious inflowing or outflowing features.

We find a tight correlation between the strong Mg II equivalent width and the host galaxy SFR at $z = 1–2$,

suggesting the coevolution of strong Mg II absorbing gas and the MSGs toward the cosmic noon. This conclusion is strengthened by the fact that the covering fraction of Mg II absorbing gas in the MSGs is two times higher than the covering fraction in all the galaxies. In particular, we detect several Mg II and C IV systems having $D/R_{\text{vir}} > 1$, indicating that the cool gas still exists out of the virial radius. This unbounded gas may be driven by the star formation activity at the cosmic noon. In Rudie et al. (2019), they found that 70% of their galaxies have some unbounded metal-enriched gas, suggesting galactic winds may commonly eject gas from halos at $z \sim 2$.

The C IV-only systems, as suggested in the COS-Halos survey in Borthakur et al. (2013) and Bordoloi et al. (2014a), likely trace the dwarf galaxies and/or starburst galaxies. The sub- L_* galaxies undergo extended bursty star formation, rather than the continuous “normal” star formation in the super- L_* galaxies. Though we do not find the host galaxies exhibit significant differences between the C IV-only systems and the C IV (with Mg II) systems. This may be due to our galaxy properties being weighted average values, representing a feature of multiple star-forming galaxies.

5.3. Environmental Effects

Environmental effects can also give rise to the optically thick cool gas. Environmental effects of the Mg II absorbing gas are detected in the MAGG survey at $z \sim 1\text{--}1.5$ (Dutta et al. 2020, 2021) and the MAGIICAT survey at $z < 1$ (Nielsen et al. 2018; Huang et al. 2021). In particular, Nielsen et al. (2018) point out that the covering fraction and median W_r of Mg II-absorbing gas residing in a group environment is larger than that of an isolated galaxy. The group environment kinematics are with more power for high-velocity dispersion, similar to outflow kinematics. Lofthouse et al. (2023) study the correlation between the $\log N(\text{H I})/\text{cm}^2 > 19$ absorbing gas and Ly α emitters at $z = 3\text{--}4$ and find that the optically thick gas covering fraction in galaxy group is three times higher than that in isolated systems.

In Chen et al. (2010a) and Huang et al. (2021), the authors find that the Mg II gas that does not show obvious anticorrelation with D resides in a group environment, rather than being associated with a single galaxy. Thus, the environmental effect is also a plausible explanation of our Mg II and C IV systems detected out of the virial radius, and no obvious anticorrelation is seen in our Mg II W_r with D/R_{vir} . Additionally, the C IV system with the largest equivalent width has three major components in the absorption profile of C IV, Mg II, and Si IV absorption. This system also has a large D/R_{vir} value (1.97), which may indicate it is affected by the outflows or reside in a group or disturbing environment.

5.4. Absorbing Gas and Nonabsorbing Gas Counterparts

In order to further test if there is an intrinsic correlation between the absorbing gas and the galaxy overdensity, we compare the galaxy density at the redshift of absorbers and nonabsorbers. In the Appendix, in Figure A2, we plot the normalized galaxy z_{phot} density $P(z)$ at $0.0 < z < 6.0$. The Mg II and C IV absorber redshifts are labeled by red and blue lines, respectively. The $P(z)$ is a normalized photo- z probability distribution, by taking around all the galaxies in the COSMOS2020 catalog within a $30''$ offset of the quasar

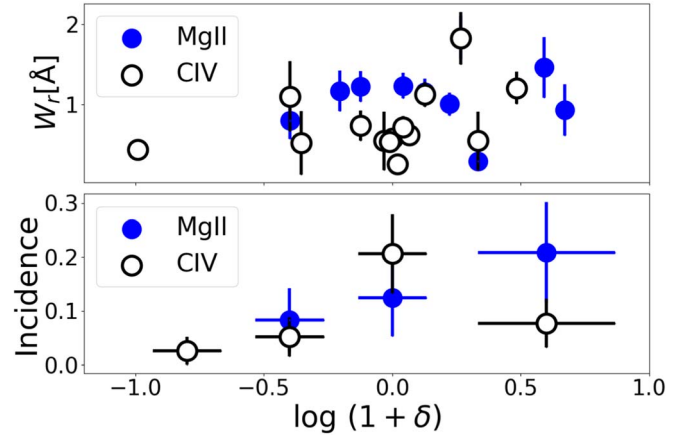


Figure 10. The cross-correlation between the Mg II and C IV incidence and equivalent width with the galaxy number overdensity δ . The p -values for the Mg II and C IV incidence with galaxy number overdensity are 0.047 and 0.590, respectively.

sightline. We find that the Mg II and Mg II (with C IV) absorbers likely occur at the redshift where the galaxy density is higher than the redshifts where there are no absorbers between $z = 1$ and 2.5. The C IV-only systems, i.e., the relatively lower $N(\text{H I})$ systems, exhibit a mild correlation with the galaxy density. We carry out a cross-correlation analysis between the incidences of Mg II and C IV absorbers and their rest-frame equivalent width W_r , with galaxy overdensity. The methodology is similar to that presented in Dutta et al. (2021). The galaxy overdensity, denoted as δ , is defined by the relation $\delta = (\rho_{\text{abs}} - \rho_0)/\rho_0$. Here, ρ_{abs} and ρ_0 are the absorbing-related and field galaxy number density, respectively. We calculate the ρ_{abs} within a velocity window of $\pm 1000 \text{ km s}^{-1}$ centered on the absorber redshift. The projected area is defined using an annulus with a radius of 250 kpc. The field galaxy number density is in a cube volume of $300 \times 300 \text{ kpc}$ and $dz = 0.2$. We plot the relation between Mg II and C IV W_r and the incidence with the galaxy number overdensity in Figure 10. From the figure, we can tell that the galaxy density is higher when the Mg II absorber incidence goes higher. We perform a Pearson correlation analysis between the Mg II and C IV incidence and the galaxy overdensity. The p -values for the Mg II and C IV incidence with galaxy number overdensity are 0.047 and 0.590, respectively. The p -values for the Mg II and C IV W_r with galaxy number overdensity are 0.838 and 0.175, respectively. This tentatively suggests that the environmental effects indeed play an active role in the origin of strong Mg II absorbing gas at the cosmic noon. We are somewhat cautious about drawing firm conclusions, given the limited sample size. The galaxy density in the large-scale structure may play a more significant role in the birth and evolution of the multiphase CGM than the specific “host” galaxy properties.

6. Summary

1. We detect 51 Mg II and 50 C IV absorption systems separately from 115 DESI SV quasars in the COSMOS+HSC fields. All of the systems having Ly α within the detection limit are with $\log N(\text{H I})/\text{cm}^2 > 14.0$. In the redshift coverage of both Mg II and C IV ($z = 1.3\text{--}2.5$), 20 out of 34 (58.82%) Mg II systems have C IV detection.

2. Fourteen quasars are covered by the COSMOS2020 catalog. By crossmatching the COSMOS2020 catalog, we

select the Mg II and C IV galaxies above the mass limit. The majority of the Mg II galaxies and C IV galaxies are classified as main-sequence star-forming galaxies within 0.3 dex scatter. A tight correlation between the Mg II equivalent width and the weighted average galaxy SFR is found. The C IV-only galaxies tentatively reside in a larger impact parameter than the systems having both Mg II and C IV absorption.

3. We find that the covering fraction of strong Mg II-absorbing gas selected galaxies in MSGs is 2 times higher than that in all the galaxy populations within 250 kpc. The strong Mg II contributes ~ 0.068 star formation to the global star formation at $z \sim 2$, which is consistent with the covering fraction of the Mg II gas. The result suggests the coevolution of cool gas probed by strong Mg II and the MSGs at the cosmic noon.

4. We find that the environmental effects and the galaxy density in a large-scale structure tentatively play an active role in the origin of multiphase CGM at $z = 1-3.0$.

Future JWST observations in the COSMOS field will also provide more information on the galaxy morphology and star formation history of host galaxies. The methods of analyzing a gaseous halo and its host galaxies in this work can be tested in the Rubin era, when a large quantity of photo- z will be provided.

Acknowledgments

We would like to thank the anonymous referee for very constructive comments. We also thank Solène Chabanier and J. Xavier Prochaska for the constructive comments in the DESI internal review. We thank Clotilde Laigle, Henry J. McCracken, John Weaver, the COSMOS team, Patrick Petitjean, Luis C. Ho, Hsiao-Wen Chen, Yunjing Wu, Ting-Wen Lan, Abhijeet Anand, Antonella Palmese, and all the colleagues at the WMAG22 conference for fruitful discussions.

S.Z., L.J., and Z.P. acknowledge support from the National Science Foundation of China (11721303, 11890693, and 12303011). S.Z., Z.C., and Z.S. are supported by the National Key R&D Program of China (grant No. 2018YFA0404503), the National Science Foundation of China (grant No.

12073014), the science research grants from the China Manned Space Project with No. CMS-CSST2021-A05, and Tsinghua University Initiative Scientific Research Program (No. 20223080023). H.Z. acknowledges support from the National Science Foundation of China (grant No. 12120101003).

This research is supported by the Director, Office of Science, Office of High Energy Physics of the U.S. Department of Energy, under Contract No. DEAC0205CH11231, and by the National Energy Research Scientific Computing Center, a DOE Office of Science User Facility, under the same contract; additional support for DESI is provided by the U.S. National Science Foundation, Division of Astronomical Sciences, under Contract No. AST-0950945 to the NSF's National Optical-Infrared Astronomy Research Laboratory; the Science and Technologies Facilities Council of the United Kingdom; the Gordon and Betty Moore Foundation; the Heising-Simons Foundation; the French Alternative Energies and Atomic Energy Commission (CEA); the National Council of Science and Technology of Mexico (CONACYT); the Ministry of Science and Innovation of Spain (MICINN); and by the DESI Member Institutions: <https://www.desi.lbl.gov/collaborating-institutions>.

The authors are honored to be permitted to conduct scientific research on Iolkam Duag (Kitt Peak), a mountain with particular significance to the Tohono Oodham Nation.

Facility: Mayall.

Appendix

In this appendix, we provide additional information on the CGM and galaxy properties in this work. Figure A1 illustrates the posterior distribution of the Pearson correlation coefficient between the Mg II and C IV absorber strength with galaxy properties. Figure A2 displays the galaxy probability density $P(z)$ as a function of redshift. Table A1 contains quasar information, including emission redshift, R.A, decl., exposure time, and S/N, used in this work. Table A2 provides details of the metal absorber measurements.

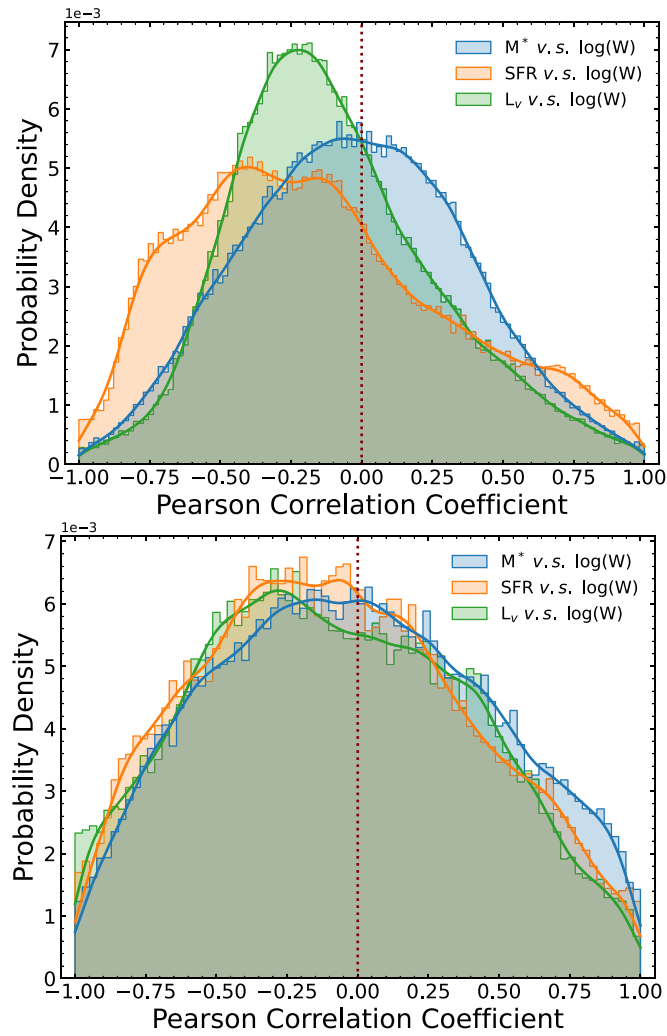


Figure A1. The posterior distribution $P(r|X)$ of the Pearson correlation coefficient r between Mg II (upper) and C IV (lower) absorber strength with galaxy properties: the $\log W_r-M_*$ (blue; $-0.03^{+0.40}_{-0.41}$, $-0.03^{+0.55}_{-0.52}$), $\log W_r-\log \text{SFR}$ (orange; $-0.20^{+0.57}_{-0.43}$, $-0.10^{+0.55}_{-0.50}$), and $\log W_r-L_v$ (green; $-0.14^{+0.42}_{-0.30}$, $-0.10^{+0.55}_{-0.48}$) relations, where X is the galaxy data set. We perform a Monte Carlo simulation to sample the data set and generate the probability density distribution.

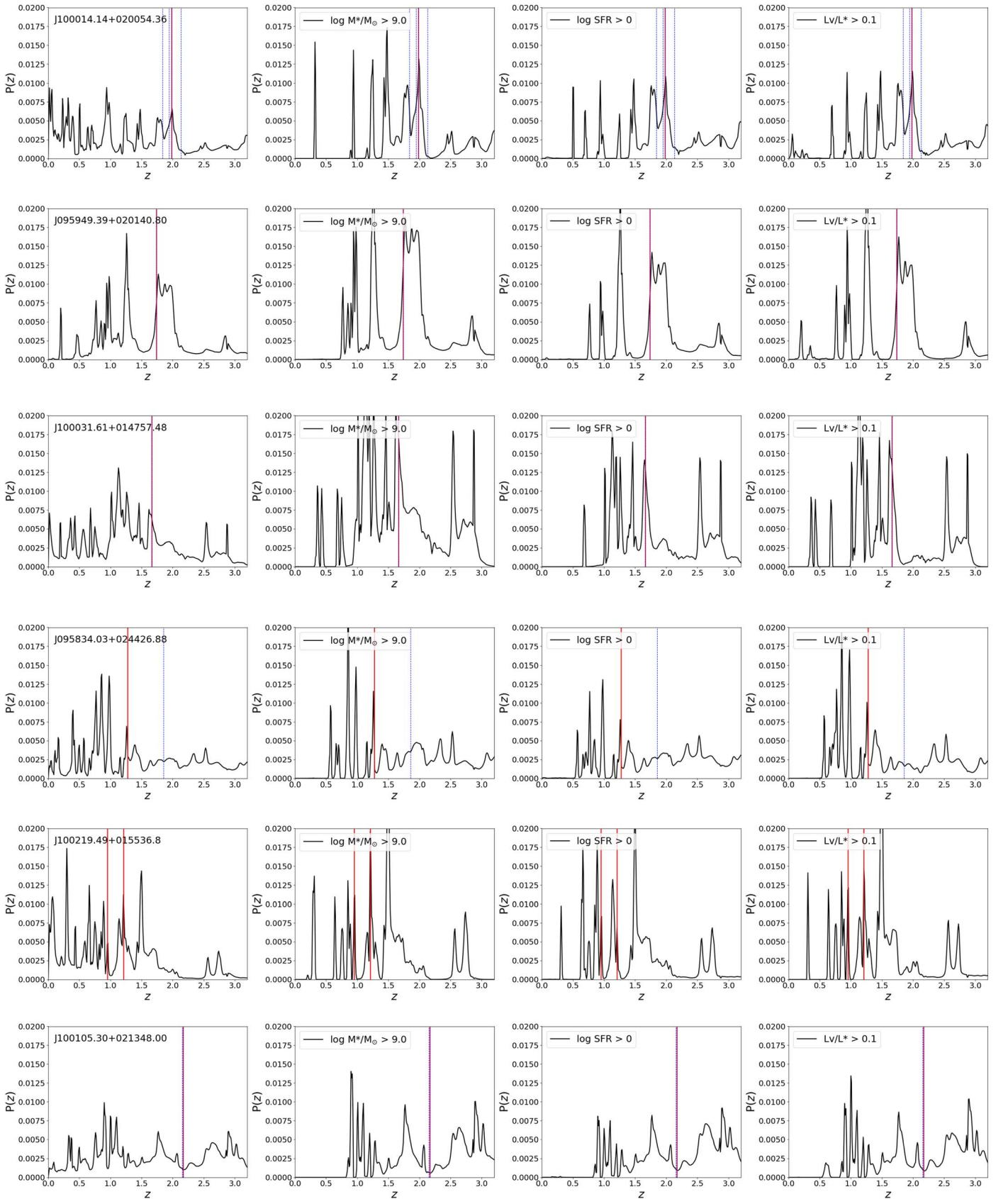


Figure A2. Galaxy probability density $P(z)$ as a function of redshift. The $P(z)$ is a normalized photometric redshift probability distribution, by taking around all the galaxies in the COSMOS2020 catalog within a $30''$ offset of the quasar sightline. The red and blue dashed lines are the absorber redshifts of the Mg II and C IV systems.

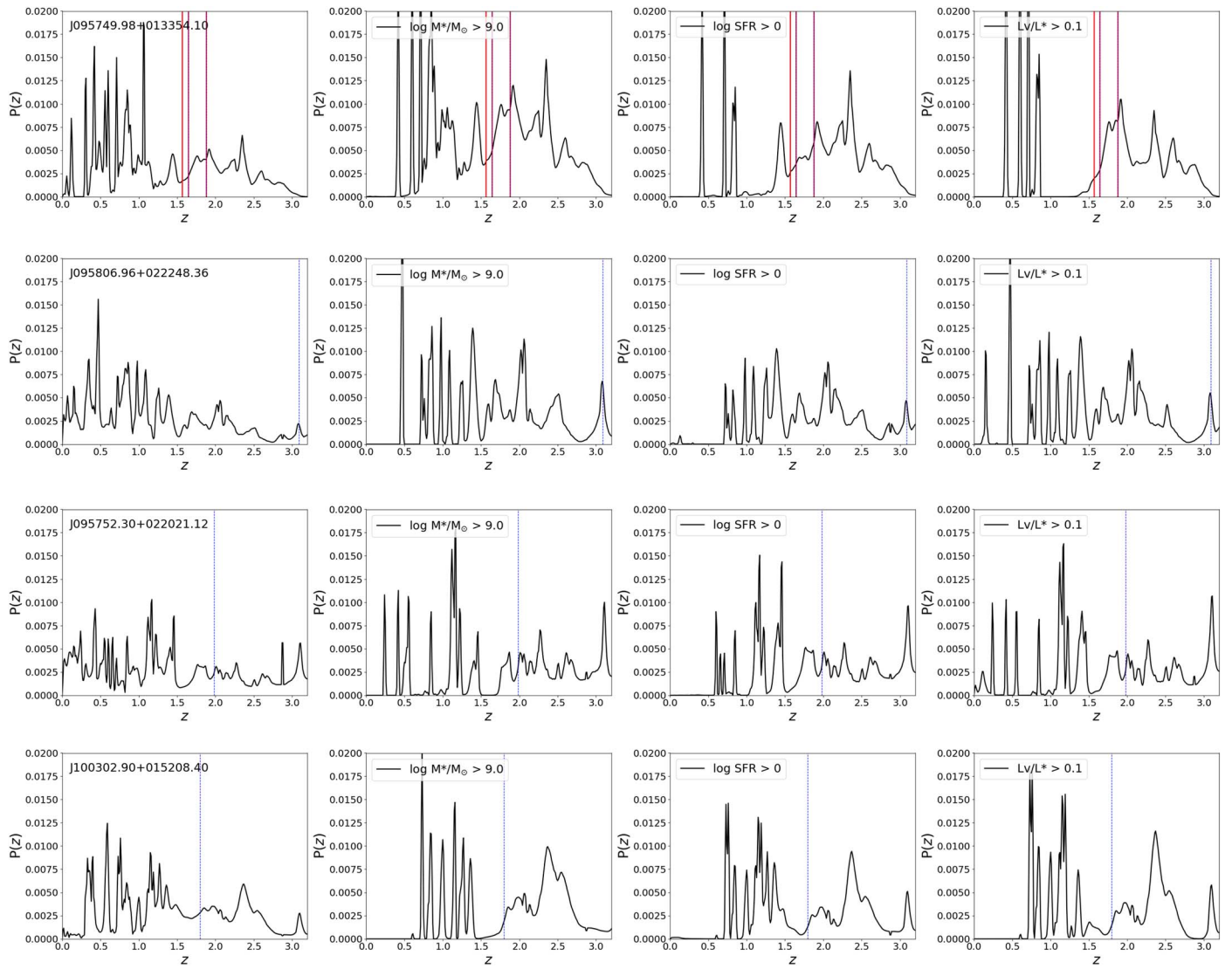


Figure A2. (Continued.)

Table A1
Quasars Used in This Work

TARGETID (1)	z_{em} (2)	R.A. (3)	Decl. (4)	EXPTIME (s) (5)	S/N (6)
J095426.83+025022.92	1.3422	148.6118	2.0897	22,884.44	8
J095430.38+021525.92	2.0498	148.6266	2.2572	7302.19	17
J095435.15+023142.24	1.3138	148.6465	2.5284	22,884.44	7
J095436.38+027031.08	1.8071	148.6516	2.1253	22,884.44	7
J095446.03+014639.00	1.1153	148.6918	1.7775	7302.19	3
J095458.24+015616.79	0.7464	148.7427	1.9380	22,884.44	29
J095504.24+026052.92	3.0927	148.7677	2.1147	22,884.44	6
J095505.44+021028.92	1.2235	148.7727	2.1747	22,884.44	4
J095525.79+028011.76	3.1414	148.8575	2.1366	2884.447	3
J095615.91+024652.67	1.6542	149.0663	2.7813	22,884.44	14
J095656.18+021314.88	1.1215	149.2341	2.2208	22,884.44	37
J095712.88+014917.39	1.1818	149.3037	1.8215	22,884.44	12
J095726.32+024027.83	0.9583	149.3597	2.0744	22,884.44	22
J095739.24+015533.23	1.8146	149.4135	1.9259	22,884.44	3
J095749.96+013353.99	2.0055	149.4582	1.5650	7302.19	18
J095752.29+022021.11	2.0490	149.4679	2.3392	7302.19	41
J095806.96+022248.36	3.0956	149.5290	2.3801	7302.19	6
J095820.44+023003.95	1.3578	149.5852	2.0511	22,884.44	36
J095834.03+024426.88	1.8927	149.6418	2.7408	7302.19	33
J095834.51+034338.63	1.2651	149.6438	3.7274	7302.19	7
J095847.11+035003.84	1.8582	149.6963	3.8344	22,884.44	15
J095900.11+033651.83	1.5873	149.7505	3.6144	7302.19	4
J095910.94+019046.80	2.6908	149.7956	1.1630	22884.44	5
J095911.63+033442.95	1.8081	149.7985	3.5786	22,884.44	3
J095915.28+034033.23	0.6818	149.8137	3.6759	7302.19	19
J095922.27+034046.56	4.0667	149.8428	3.6796	7302.19	3
J095923.80+003853.16	0.7838	149.8492	0.6481	7302.19	3
J095931.72+033710.19	1.1300	149.8822	3.6195	6402.13	4
J095933.12+033118.12	2.1464	149.8880	3.5217	7302.19	6
J095946.82+004918.47	2.2488	149.9451	0.8218	22,884.44	70
J095949.39+021040.80	1.7533	149.9558	2.0280	7302.19	26
J095956.56+004301.55	1.9471	149.9857	0.7171	7302.19	4
J100009.35+005311.03	0.9103	150.0390	0.8864	22,884.44	6
J100011.59+004154.24	1.3761	150.0483	0.6984	7302.19	3
J100014.13+020054.35	2.4968	150.0589	2.0151	22,884.44	32
J100017.87+005400.00	0.7289	150.0745	0.9000	7302.19	5
J100020.49+015011.40	1.5242	150.0854	1.0865	22,884.44	8
J100020.49+033247.76	2.0233	150.0854	3.5466	22,884.44	3
J100022.72+033724.96	0.9057	150.0947	3.6236	7302.19	6
J100023.78+035500.12	1.1259	150.0991	3.9167	22,884.44	16
J100025.32+034823.76	2.4103	150.1055	3.8066	22,884.44	15
J100029.13+011044.75	1.0591	150.1214	1.0291	7302.19	37
J100029.68+035023.27	1.6433	150.1237	3.0898	22,884.44	21
J100031.60+014757.47	1.683	150.1317	1.7993	22,884.44	17
J100032.80+033458.43	1.724	150.1367	3.5829	7302.19	6
J100036.98+018003.12	1.8355	150.1541	1.1342	7302.19	3
J100037.39+034455.68	3.2336	150.1558	3.7488	7302.19	15
J100038.47+015009.24	2.1797	150.1603	1.0859	22,884.44	9
J100039.23+012006.35	3.8343	150.1635	1.0351	7302.19	5
J100039.55+033216.44	0.9768	150.1648	3.5379	22,884.44	11
J100042.11+034911.27	1.6542	150.1755	3.8198	22,884.44	12
J100042.98+004438.76	1.452	150.1791	0.7441	7302.19	5
J100043.39+033217.16	2.2667	150.1808	3.5381	22,884.44	3
J100047.92+034700.95	1.9006	150.1997	3.7836	7302.19	3
J100048.83+005925.79	0.8704	150.2035	0.9905	7302.19	3
J100048.83+033039.23	3.3652	150.2035	3.5109	22,884.44	7
J100052.29+005121.59	1.9461	150.2179	0.8560	7302.19	7
J100053.80+033105.87	2.4587	150.2242	3.5183	22,884.44	3
J100055.00+005508.40	2.0652	150.2292	0.9190	7302.19	5
J100058.53+004837.44	1.7392	150.2439	0.8104	7302.19	3
J100058.82+015359.99	1.5619	150.2451	1.9000	7302.19	16
J100101.03+035233.96	2.7714	150.2543	3.8761	22,884.44	1
J100104.60+004648.00	2.5726	150.2692	0.7800	7302.19	3

Table A1
(Continued)

TARGETID (1)	z_{em} (2)	R.A. (3)	Decl. (4)	EXPTIME (s) (5)	S/N (6)
J100105.30+021347.99	2.6066	150.2721	2.2300	7302.19	8
J100106.43+033650.39	2.0931	150.2768	3.6140	7302.19	4
J100108.66+005730.59	2.0411	150.2861	0.9585	7302.19	25
J100109.21+004859.40	0.6574	150.2884	0.8165	7302.19	8
J100111.40+034100.23	2.2668	150.2975	3.6834	7302.19	29
J100111.49+033506.36	2.4574	150.2979	3.5851	7302.19	21
J100113.39+005009.95	2.5853	150.3058	0.8361	7302.19	4
J100118.31+035101.07	2.8947	150.3263	3.8503	22,884.44	6
J100125.46+005205.15	0.7802	150.3561	0.8681	22,884.44	56
J100126.59+004648.71	1.7273	150.3608	0.7802	7302.19	8
J100127.55+034434.07	2.8133	150.3648	3.7428	22,884.44	22
J100129.44+003813.55	2.9074	150.3727	0.6371	4602.01	3
J100132.08+005259.15	1.0669	150.3837	0.8831	22,884.44	8
J100133.36+005118.71	1.403	150.3890	0.8552	22,884.44	11
J100134.15+011021.72	1.7589	150.3923	1.1727	7302.19	3
J100136.36+034309.48	1.1248	150.4015	3.7193	5502.06	5
J100137.19+021612.35	1.65	150.4050	2.2701	2884.447	11
J100137.77+004655.56	2.5841	150.4074	0.7821	7302.19	25
J100138.97+033616.19	1.2473	150.4124	3.6045	7302.19	10
J100140.31+003947.52	1.6027	150.4180	0.6632	7302.19	4
J100142.04+003907.55	1.3516	150.4252	0.6521	7302.19	3
J100142.55+015031.20	1.8225	150.4273	1.0920	7302.19	6
J100147.88+021447.03	0.8804	150.4495	2.2464	22,884.44	17
J100205.23+004249.68	1.7855	150.5218	0.7138	7302.19	11
J100217.87+004252.20	1.2343	150.5745	0.7145	7302.19	10
J100219.48+015536.84	1.5087	150.5812	1.9269	7302.19	17
J100236.69+015948.47	1.5192	150.6529	1.9968	7302.19	19
J100302.90+015208.40	1.8026	150.7621	1.8690	7302.19	22
J100344.35+025002.03	2.9914	150.9348	2.0839	7302.19	8
J100348.67+021044.76	1.3908	150.9528	2.1791	7302.19	4
J100417.61+021330.35	3.1056	151.0734	2.2251	22,884.44	3
J100441.78+021147.04	1.828	151.1741	2.1964	22,884.44	6
J100449.99+021641.52	1.7882	151.2083	2.2782	22,884.44	3
J100505.03+021519.08	2.8624	151.2710	2.2553	22,884.44	9
J100520.87+021112.84	2.3843	151.3370	2.1869	7302.19	7
J100523.85+015920.40	1.7769	151.3494	1.9890	22,884.44	18
J100524.86+025047.76	1.0844	151.3536	2.0966	22,884.44	6
J100527.09+027025.31	1.5706	151.3629	2.1237	22,884.44	5
J100534.43+021015.96	1.8209	151.3935	2.1711	7302.19	18
J100541.51+015950.64	1.7298	151.4230	1.9974	22,884.44	16
J100542.69+021516.92	1.1336	151.4279	2.2547	22,884.44	4
J100546.20+027052.67	1.7086	151.4425	2.1313	22,884.44	4
J100547.68+021221.59	0.9066	151.4487	2.2060	22,884.44	11
J100606.45+021445.23	1.1864	151.5269	2.2459	22,884.44	6
J100624.45+014758.20	1.0138	151.6019	1.7995	22,884.44	4
J100632.71+013955.43	2.4867	151.6363	1.6654	6402.13	3
J100634.60+026014.40	2.3479	151.6442	2.1040	7302.19	3
J100638.88+014941.16	2.1134	151.6620	1.8281	7302.19	3
J100641.11+021658.07	2.0098	151.6713	2.2828	22,884.44	17
J100039.25+010206.47	3.8344	150.1635	1.0350	7302.19	18
J100015.90+010801.75	2.0098	151.6713	2.2828	22,884.44	17

Notes. Column (1): quasar name. Column (2): quasar emission redshift. Column (3): R.A. Column (4): decl. Column (5): quasar effective exposure time. Column (6): mean S/N measured from the three continuum regions without obvious emission or absorption.

Table A2
Metal Absorber Measurements

TARGETID	z_{abs}	$\Delta v(\lambda 2796)$ (km s^{-1})	$W_r(\lambda 2796)$ (\AA)	$\Delta v(\lambda 1548)$ (km s^{-1})	$W_r(\lambda 1548)$ (\AA)
(1)	(2)	(3)	(4)	(5)	(6)
J100219.48+015536.84	0.9520	495.462	1.462 ± 0.316
J100219.48+015536.84	1.2090	206.951	0.631 ± 0.096
J100302.90+015208.40	1.7970	411.110	0.533 ± 0.091
J095749.96+013353.99	1.6428	379.000	1.223 ± 0.162	419.351	0.738 ± 0.2
J095749.96+013353.99	1.5660	465.260	1.169 ± 0.202	375.754	0.716 ± 0.142
J095749.96+013353.99	1.8770	314.938	1.234 ± 0.114
J095834.03+024426.88	1.2756	393.437	1.005 ± 0.126
J095820.44+023003.95	0.7505	480.986	0.9 ± 0.087
J095808.15+015425.20	2.4845	119.614	1.676 ± 0.666
J100113.39+005009.95	1.0620	294.506	1.853 ± 0.636
J100137.77+004655.56	2.1385	528.224	1.656 ± 0.278
J100137.77+004655.56	1.3445	235.737	0.41 ± 0.108
J100205.23+004249.68	1.2510	410.364	1.286 ± 0.392
J100039.25+010206.47	1.3450	219.637	0.74 ± 0.385
J100108.66+005730.59	2.0250	402.453	0.386 ± 0.065
J100108.66+005730.59	1.7378	486.468	0.570 ± 0.196	449.654	0.503 ± 0.193
J095430.38+021525.92	1.8315	636.834	0.636 ± 0.43	364.219	0.84 ± 0.189
J095430.38+021525.92	1.1072	336.301	0.346 ± 0.22
J100111.40+034100.23	2.2660	606.366	1.114 ± 0.055
J100111.40+034100.23	1.4660	976.981	0.625 ± 0.408
J100111.40+034100.23	1.5475	431.816	0.476 ± 0.157
J100111.40+034100.23	1.6715	352.731	0.336 ± 0.139
J100534.43+021015.96	1.4990	693.396	4.891 ± 0.283
J100534.43+021015.96	1.1940	391.394	0.719 ± 0.195
J100111.49+033506.36	1.4140	643.073	0.504 ± 0.217
J100111.49+033506.36	0.6605	785.408	0.728 ± 0.36
J100111.49+033506.36	1.4140	444.960	0.712 ± 0.16
J100541.51+015950.64	0.8280	420.354	0.908 ± 0.278
J100541.51+015950.64	1.4480	316.473	1.408 ± 0.155	451.940	1.444 ± 0.268
J100527.09+027025.31	1.4846	360.323	1.699 ± 0.574	464.818	1.591 ± 0.559
J100042.11+034911.27	1.6425	544.964	2.611 ± 0.141	610.488	1.907 ± 0.261
J095946.82+004918.47	2.1544	359.402	0.399 ± 0.034	482.318	0.227 ± 0.043
J095847.11+035003.84	1.3310	453.723	0.856 ± 0.203
J100025.32+034823.76	1.5140	349.751	0.741 ± 0.205	374.901	0.627 ± 0.079
J100029.68+035023.27	0.9760	423.160	1.01 ± 0.196
J100217.87+004252.20	1.2230	213.961	0.274 ± 0.149
J100015.90+010801.75	1.4780	312.211	2.061 ± 0.8
J100632.71+013955.43	2.4886	146.668	0.848 ± 0.249
J095949.39+021040.80	1.7372	530.321	1.152 ± 0.175	522.252	1.126 ± 0.08
J100058.82+015359.99	0.6715	603.396	2.235 ± 0.36
J100105.30+021347.99	2.1680	585.025	1.102 ± 0.421
J100105.30+021347.99	2.1530	212.247	0.799 ± 0.212	478.487	0.518 ± 0.341
J100014.13+020054.35	1.4700	241.531	0.804 ± 0.332
J100133.36+005118.71	0.7838	580.924	1.552 ± 0.531
J100031.60+014757.47	1.6625	689.316	1.836 ± 0.257	722.683	1.828 ± 0.27
J095426.83+025022.92	1.3500	403.319	1.279 ± 0.253	504.614	0.877 ± 0.281
J095726.32+024027.83	0.7575	381.720	0.622 ± 0.158
J100014.13+020054.35	2.1305	395.208	0.434 ± 0.071
J100014.13+020054.35	1.9813	342.842	0.300 ± 0.117	514.078	0.453 ± 0.148
J100014.13+020054.35	1.9450	558.430	0.62 ± 0.099
J100014.13+020054.35	1.8400	568.266	0.574 ± 0.147
J100137.19+021612.35	1.6360	497.133	2.682 ± 0.205	669.046	2.911 ± 0.99
J100441.78+021147.04	1.4015	416.102	1.794 ± 0.521
J095435.15+023142.24	1.3010	443.636	1.971 ± 0.336
J100127.55+034434.07	2.7740	422.899	1.34 ± 0.09
J100127.55+034434.07	2.2294	284.891	0.327 ± 0.122	468.897	1.08 ± 0.125
J100055.00+005508.40	1.9490	447.044	1.538 ± 0.517
J095752.29+022021.11	1.9810	523.836	0.546 ± 0.210
J095834.03+024426.88	1.8555	508.977	0.252 ± 0.103
J095826.64+024228.00	2.4520	482.868	0.923 ± 0.296
J095839.84+024424.00	3.1620	220.482	0.530 ± 0.100
J095839.84+024424.00	3.1800	152.901	0.217 ± 0.100

Table A2
(Continued)

TARGETID	z_{abs}	$\Delta v(\lambda 2796)$ (km s^{-1})	$W_r(\lambda 2796)$ (\AA)	$\Delta v(\lambda 1548)$ (km s^{-1})	$W_r(\lambda 1548)$ (\AA)
(1)	(2)	(3)	(4)	(5)	(6)
J100038.47+015009.24	2.1774	510.516	1.124 ± 0.121
J100104.60+004648.00	2.5350	602.860	3.052 ± 0.991
J100129.44+003813.55	2.9100	515.093	1.92 ± 0.482
J100055.00+005508.40	2.0710	464.685	1.506 ± 0.271
J100638.88+014941.16	2.1080	323.381	0.922 ± 0.214
J100344.35+025002.03	3.0290	481.671	1.477 ± 0.258
J095806.96+022248.36	3.0880	369.762	1.207 ± 0.211
J095933.12+033118.12	2.1020	504.720	1.098 ± 0.35
J095933.12+033118.12	2.1320	248.939	0.859 ± 0.217	581.047	1.143 ± 0.202
J100037.39+034455.68	2.8240	400.547	0.56 ± 0.123
J095504.24+026052.92	2.2050	347.999	0.694 ± 0.103
J095436.38+027031.08	1.7950	721.820	2.092 ± 0.246
J095525.79+028011.76	3.1390	261.151	0.684 ± 0.133
J100449.99+021641.52	1.7362	457.749	1.303 ± 0.137
J100020.49+033247.76	2.0110	360.158	1.18 ± 0.639
J100043.39+033217.16	2.2674	480.610	1.871 ± 0.278

Notes. Column (1): quasar name. Column (2): absorber redshift. Column (3): velocity width of Mg II ($\lambda 2796$) line. Column (4): equivalent width of Mg II ($\lambda 2796$) line. Column (5): velocity width of C IV ($\lambda 1548$) line. Column (6): equivalent width of C IV ($\lambda 1548$) line.

ORCID iDs

Siwei Zou  <https://orcid.org/0000-0002-3983-6484>
 Linhua Jiang  <https://orcid.org/0000-0003-4176-6486>
 Zheng Cai  <https://orcid.org/0000-0001-8467-6478>
 John Moustakas  <https://orcid.org/0000-0002-2733-4559>
 Zechang Sun  <https://orcid.org/0000-0002-8246-7792>
 Zhiwei Pan  <https://orcid.org/0000-0003-0230-6436>
 Jiani Ding  <https://orcid.org/0000-0003-4651-8510>
 Jaime E. Forero-Romero  <https://orcid.org/0000-0002-2890-3725>
 Hu Zou  <https://orcid.org/0000-0002-6684-3997>
 Yuan-sen Ting  <https://orcid.org/0000-0001-5082-9536>
 Steven Ahlen  <https://orcid.org/0000-0001-6098-7247>
 David Alexander  <https://orcid.org/0000-0002-5896-6313>
 David Brooks  <https://orcid.org/0000-0002-8458-5047>
 Arjun Dey  <https://orcid.org/0000-0002-4928-4003>
 Andreu Font-Ribera  <https://orcid.org/0000-0002-3033-7312>
 Satya Gontcho A. Gontcho  <https://orcid.org/0000-0003-3142-233X>
 Klaus Honscheid  <https://orcid.org/0000-0002-6550-2023>
 Martin Landriau  <https://orcid.org/0000-0003-1838-8528>
 Mariana Vargas Magana  <https://orcid.org/0000-0003-3841-1836>
 Aaron Meisner  <https://orcid.org/0000-0002-1125-7384>
 Ramon Miquel  <https://orcid.org/0000-0002-6610-4836>
 Michael Schubnell  <https://orcid.org/0000-0001-9504-2059>
 Gregory Tarlé  <https://orcid.org/0000-0003-1704-0781>
 Zhimin Zhou  <https://orcid.org/0000-0002-4135-0977>

References

- Aihara, H., Armstrong, R., Bickerton, S., et al. 2018, *PASJ*, 70, S8
 Alexander, D. M., Davis, T. M., Chaussidon, E., et al. 2023, *AJ*, 165, 124
 Arnouts, S., Moscardini, L., Vanzella, E., et al. 2002, *MNRAS*, 329, 355
 Bergeron, J., & Boissé, P. 1991, *A&A*, 243, 344
 Bordoloi, R., Lilly, S. J., Kacprzak, G. G., & Churchill, C. W. 2014a, *ApJ*, 784, 108
 Bordoloi, R., Tumlinson, J., Werk, J. K., et al. 2014b, *ApJ*, 796, 136
 Bordoloi, R., Lilly, S. J., Knobel, C., et al. 2011, *ApJ*, 743, 10
 Borthakur, S., Heckman, T., Strickland, D., Wild, V., & Schiminovich, D. 2013, *ApJ*, 768, 18
 Bouché, N., Murphy, M. T., Péroux, C., Csabai, I., & Wild, V. 2006, *MNRAS*, 371, 495
 Brammer, G. B., van Dokkum, P. G., & Coppi, P. 2008, *ApJ*, 686, 1503
 Bruzual, G., & Charlot, S. 2003, *MNRAS*, 344, 1000
 Burchett, J. N., Tripp, T. M., Bordoloi, R., et al. 2016, *ApJ*, 832, 124
 Busca, N., & Balland, C. 2018, arXiv:1808.09955
 Cai, Z., Fan, X., Yang, Y., et al. 2017a, *ApJ*, 837, 71
 Cai, Z., Fan, X., Bian, F., et al. 2017b, *ApJ*, 839, 131
 Cai, Z., Cantalupo, S., Prochaska, J. X., et al. 2019, *ApJS*, 245, 23
 Cantalupo, S., Arrighi-Battaia, F., Prochaska, J. X., Hennawi, J. F., & Madau, P. 2014, *Natur*, 506, 63
 Chaussidon, E., Yèche, C., Palanque-Delabrouille, N., et al. 2023, *ApJ*, 944, 107
 Chen, H.-W., Helsby, J. E., Gauthier, J.-R., et al. 2010a, *ApJ*, 714, 1521
 Chen, H.-W., Wild, V., Tinker, J. L., et al. 2010b, *ApJL*, 724, L176
 Chen, S.-F. S., Simcoe, R. A., Torrey, P., et al. 2017, *ApJ*, 850, 188
 Churchill, C. W., Mellon, R. R., Charlton, J. C., et al. 2000, *ApJS*, 130, 91
 Churchill, C. W., Nielsen, N. M., Kacprzak, G. G., & Trujillo-Gomez, S. 2013a, *ApJL*, 763, L42
 Churchill, C. W., Trujillo-Gomez, S., Nielsen, N. M., & Kacprzak, G. G. 2013b, *ApJ*, 779, 87
 DeFelippis, D., Genel, S., Bryan, G. L., et al. 2020, *ApJ*, 895, 17
 DESI Collaboration, Aghamousa, A., Aguilar, J., et al. 2016a, arXiv:1611.00036
 DESI Collaboration, Aghamousa, A., Aguilar, J., et al. 2016b, arXiv:1611.00037
 DESI Collaboration, Adame, A. G., Aguilar, J., et al. 2023a, arXiv:2306.06308
 DESI Collaboration, Adame, A. G., Aguilar, J., et al. 2023b, arXiv:2306.06307
 DESI Collaboration, Abareschi, B., Aguilar, J., et al. 2022, *AJ*, 164, 207
 Dutta, R., Fumagalli, M., Fossati, M., et al. 2020, *MNRAS*, 499, 5022
 Dutta, R., Fumagalli, M., Fossati, M., et al. 2021, *MNRAS*, 508, 4573
 Farr, J., Font-Ribera, A., & Pontzen, A. 2020, *JCAP*, 2020, 015
 Feltre, A., Bacon, R., Tresse, L., et al. 2018, *A&A*, 617, A62
 Ford, A. B., Oppenheimer, B. D., Davé, R., et al. 2013, *MNRAS*, 432, 89
 Fossati, M., Fumagalli, M., Lofthouse, E. K., et al. 2021, *MNRAS*, 503, 3044
 Girelli, G., Pozzetti, L., Bolzonella, M., et al. 2020, *A&A*, 634, A135
 Guo, H., Shen, Y., & Wang, S., 2018 PyQSOFit: Python code to fit the spectrum of quasars, Astrophysics Source Code Library, ascl:1809.008
 Guy, J., Bailey, S., Kremin, A., et al. 2023, *AJ*, 165, 144
 Huang, Y.-H., Chen, H.-W., Shectman, S. A., et al. 2021, *MNRAS*, 502, 4743
 Ilbert, O., Arnouts, S., McCracken, H. J., et al. 2006, *A&A*, 457, 841
 Joshi, R., Srianand, R., Noterdaeme, P., & Petitjean, P. 2017, *MNRAS*, 465, 701
 Krogager, J.-K. 2018, arXiv:1803.01187

- Krogager, J.-K., Møller, P., Fynbo, J. P. U., & Noterdaeme, P. 2017, *MNRAS*, **469**, 2959
- Laigle, C., McCracken, H. J., Ilbert, O., et al. 2016, *ApJS*, **224**, 24
- Lan, T.-W. 2020, *ApJ*, **897**, 97
- Lan, T.-W., Tojeiro, R., Armengaud, E., et al. 2023, *ApJ*, **943**, 68
- Leclercq, F., Verhamme, A., Epinat, B., et al. 2022, *A&A*, **663**, A11
- Ledoux, C., Noterdaeme, P., Petitjean, P., & Srianand, R. 2015, *A&A*, **580**, A8
- Lin, X., Cai, Z., Zou, S., et al. 2023, *ApJL*, **944**, L59
- Lofthouse, E. K., Fumagalli, M., Fossati, M., et al. 2023, *MNRAS*, **518**, 305
- Lyke, B. W., Higley, A. N., McLane, J. N., et al. 2020, *ApJS*, **250**, 8
- Madau, P., & Dickinson, M. 2014, *ARA&A*, **52**, 415
- Martin, D. C., Chang, D., Matuszewski, M., et al. 2014, *ApJ*, **786**, 106
- Ménard, B., Wild, V., Nestor, D., et al. 2011, *MNRAS*, **417**, 801
- Myers, A. D., Moustakas, J., Bailey, S., et al. 2023, *AJ*, **165**, 50
- Napolitano, L., Pandey, A., Myers, A. D., et al. 2023, *AJ*, **166**, 99
- Neeleman, M., Bañados, E., Walter, F., et al. 2019, *ApJ*, **882**, 10
- Nelson, D., Sharma, P., Pillepich, A., et al. 2020, *MNRAS*, **498**, 2391
- Nestor, D. B., Johnson, B. D., Wild, V., et al. 2011, *MNRAS*, **412**, 1559
- Nielsen, N. M., Churchill, C. W., & Kacprzak, G. G. 2013a, *ApJ*, **776**, 115
- Nielsen, N. M., Churchill, C. W., Kacprzak, G. G., & Murphy, M. T. 2013b, *ApJ*, **776**, 114
- Nielsen, N. M., Kacprzak, G. G., Pointon, S. K., Churchill, C. W., & Murphy, M. T. 2018, *ApJ*, **869**, 153
- Noterdaeme, P., Ledoux, C., Zou, S., et al. 2018, *A&A*, **612**, A58
- Noterdaeme, P., Petitjean, P., Srianand, R., Ledoux, C., & López, S. 2011, *A&A*, **526**, L7
- Oppenheimer, B. D., & Davé, R. 2008, *MNRAS*, **387**, 577
- Pâris, I., Petitjean, P., Rollinde, E., et al. 2011, *A&A*, **530**, A50
- Péroux, C., & Howk, J. C. 2020, *ARA&A*, **58**, 363
- Petitjean, P., Srianand, R., & Ledoux, C. 2000, *A&A*, **364**, L26
- Pieri, M. M., Mortonson, M. J., Frank, S., et al. 2014, *MNRAS*, **441**, 1718
- Prochaska, J. X., Chen, H.-W., Wolfe, A. M., Dessauges-Zavadsky, M., & Bloom, J. S. 2008, *ApJ*, **672**, 59
- Prochter, G. E., Prochaska, J. X., & Burles, S. M. 2006, *ApJ*, **639**, 766
- Rafelski, M., Wolfe, A. M., Prochaska, J. X., Neeleman, M., & Mendez, A. J. 2012, *ApJ*, **755**, 89
- Raichoor, A., Moustakas, J., Newman, J. A., et al. 2023, *AJ*, **165**, 126
- Rubin, K. H. R., Diamond-Stanic, A. M., Coil, A. L., Crighton, N. H. M., & Moustakas, J. 2018, *ApJ*, **853**, 95
- Rudie, G. C., Steidel, C. C., Pettini, M., et al. 2019, *ApJ*, **885**, 61
- Rudie, G. C., Steidel, C. C., Trainor, R. F., et al. 2012, *ApJ*, **750**, 67
- Schroetter, I., Bouché, N. F., Zabl, J., et al. 2019, *MNRAS*, **490**, 4368
- Schroetter, I., Bouché, N. F., Zabl, J., et al. 2021, *MNRAS*, **506**, 1355
- Scoville, N., Aussel, H., Benson, A., et al. 2007, *ApJS*, **172**, 150
- Speagle, J. S., Steinhardt, C. L., Capak, P. L., & Silverman, J. D. 2014, *ApJS*, **214**, 15
- Steidel, C. C., Kollmeier, J. A., Shapley, A. E., et al. 2002, *ApJ*, **570**, 526
- Sun, Z., Ting, Y.-S., & Cai, Z. 2023, *ApJS*, **269**, 4
- Suresh, J., Rubin, K. H. R., Kannan, R., et al. 2017, *MNRAS*, **465**, 2966
- Tumlinson, J., Peebles, M. S., & Werk, J. K. 2017, *ARA&A*, **55**, 389
- Weaver, J. R., Kauffmann, O. B., Ilbert, O., et al. 2022, *ApJS*, **258**, 11
- Welsh, L., Cooke, R., Fumagalli, M., & Pettini, M. 2022, *ApJ*, **929**, 158
- Wolfe, A. M., Gawiser, E., & Prochaska, J. X. 2005, *ARA&A*, **43**, 861
- Yang, J., Fan, X., Gupta, A., et al. 2023, *ApJS*, **269**, 27
- Yèche, C., Palanque-Delabrouille, N., Claveau, C.-A., et al. 2020, *RNAAS*, **4**, 179
- Zabl, J., Bouché, N. F., Schroetter, I., et al. 2019, *MNRAS*, **485**, 1961
- Zhou, R., Dey, B., Newman, J. A., et al. 2023, *AJ*, **165**, 58
- Zhu, G., & Ménard, B. 2013, *ApJ*, **770**, 130
- Zou, S., Petitjean, P., Noterdaeme, P., et al. 2018, *A&A*, **616**, A158
- Zou, S., Petitjean, P., Noterdaeme, P., et al. 2020, *ApJ*, **901**, 105
- Zou, S., Jiang, L., Shen, Y., et al. 2021, *ApJ*, **906**, 32